iScience

CellPress
OPEN ACCESS

Article

Complete Photocatalytic Mineralization of Microplastic on TiO_2 Nanoparticle Film

Iqra Nabi, Aziz-Ur-Rahim Bacha, Kejian Li, ..., Yang Yang, Yiqing Feng, Liwu Zhang

zhanglw@fudan.edu.cn

HIGHLIGHTS

Efficient degradation of microplastics under UV light by TiO_2 film

Triton-based TiO_2 film showed higher photocatalytic performance

The role of radical species during microplastics degradation was elucidated

Degradation mechanism and reaction intermediates were explored

Nabi et al., iScience 23, 101326
July 24, 2020
https://doi.org/10.1016/j.isci.2020.101326

iScience

CellPress
OPEN ACCESS

Article

Complete Photocatalytic Mineralization of Microplastic on TiO_2 Nanoparticle Film

Iqra Nabi,[1] Aziz-Ur-Rahim Bacha,[1] Kejian Li,[1] Hanyun Cheng,[1] Tao Wang,[1] Yangyang Liu,[1] Saira Ajmal,[1] Yang Yang,[1] Yiqing Feng,[1] and Liwu Zhang[1,2,*]

SUMMARY

Recently, the environmental impacts of microplastics have received extensive attention owing to their accumulation in the environment. However, developing efficient technology for the control and purification of microplastics is still a big challenge. Herein, we investigated the photocatalytic degradation of typical microplastics such as polystyrene (PS) microspheres and polyethylene (PE) over TiO_2 nanoparticle films under UV light irradiation. TiO_2 nanoparticle film made with Triton X-100 showed complete mineralization (98.40%) of 400-nm PS in 12 h, while degradation for varying sizes of PS was also studied. PE degradation experiment presented a high photodegradation rate after 36 h. CO_2 was found as the main end product. The degradation mechanism and intermediates were studied by *in situ* DRIFTS and HPPI-TOFMS, showing the generation of hydroxyl, carbonyl, and carbon-hydrogen groups during the photodegradation of PS. This study provides a green and cost-efficient strategy for the control of microplastics contamination in the environment.

INTRODUCTION

Plastics are an ideal choice owing to its light weight, low cost, and high durability; nevertheless, their use still leads to the ever-widening problem of disposal. More than 8×10^9 metric tons of plastic reaches the waterbodies every single year, and pollution is expected to surpass oceanic fish in the next coming years (MacArthur, 2017). Generally, the discharged plastics debased into small particles via combined effects of solar irradiation, physical degradation, and biodegradation (van Weert et al., 2019). The plastic decomposition leads to the formation of the micro (size less than 5 μm) and nano-plastics (size less than 1 μm) (Koelmans et al., 2015). Although recycling is progressively predominant, one-third of all plastics are still small or complex to recuperate economically (Garcia and Robertson, 2017). As a conventional plastic material, polystyrene (PS) and polyethylene (PE) are used in building materials (insulation and molding), foam packaging, food containers, and compact disks (Zan et al., 2004). However, their release in the water environment occurs through poor handling, wastewater treatment plants (McCormick et al., 2014), and microbial decomposition (Andrady, 2011). PS and PE show adverse effects on human health and aquatic organisms owing to their recalcitrant nature (Li et al., 2018). Its contamination within the aquatic environment poses a severe threat not only to aquatic biota but also to terrestrial organisms via food webs (Barboza et al., 2018; Besseling et al., 2012; Fossi et al., 2014; Rochman et al., 2017; Watts et al., 2014). The seriousness and complication of plastics waste problems indicate that a new approach is desperately required for the decomposition of polymers.

The conventional wastewater purification technologies present difficulty in control and elimination of microplastics (Moore, 2008). Several techniques have been used for the removal of microplastics, including biodegradation (Rochman et al., 2017; Yang et al., 2015) and photodegradation (Feng et al., 2010). The biodegradation process is highly dependent on the microbial species and soil environment and requires more stringent storage conditions (Inkinen et al., 2011; Jakubowicz, 2003). Feng and his coworkers first time reported the photo-assisted Fenton degradation of polystyrene microspheres (Feng et al., 2010), whereas other studies on polystyrene degradation mainly dealt with plastic film for the development of photodegradable plastics (Kemp and McIntyre, 2006; Shang et al., 2003; Zan et al., 2006). The main limitation of Fenton-based reaction is the oxidant and iron ions loss due to the radical scavenging effect of hydrogen peroxide (H_2O_2) (Zhou et al., 2016). Recently, Kang et al. studied the degradation of cosmetic

[1]Shanghai Key Laboratory of Atmospheric Particle Pollution and Prevention, Department of Environmental Science & Engineering, Fudan University, Shanghai 200433, China

[2]Shanghai Institute of Pollution Control and Ecological Security, Shanghai 200092, China

*Correspondence: zhanglw@fudan.edu.cn

https://doi.org/10.1016/j.isci.2020.101326

microplastics by catalytic activation of peroxymonosulfate to generate reactive radicals using carbon hybrids (Kang et al., 2019). However, the complete mineralization of microplastics was not achieved.

Photocatalysis is considered as an advanced oxidation process for pollutants removal (Klavarioti et al., 2009). It is a well-established green technique with a primary feature that it exploits free and infinite solar energy, implying its great potential as a low-cost and environmentally friendly treatment technology (Li et al., 2019). TiO_2 is widely used as a model photocatalyst owing to its efficient oxidizing ability of organic pollutants (Yuan et al., 2017). TiO_2 has performed exceptionally well in various studies for the removal of organic pollutants under UV light, and there is a need to further study its use for microplastic degradation, although few studies have used TiO_2/plastic composite materials for the development of photodegradable plastic (Kemp and McIntyre, 2006; Shang et al., 2003; Zan et al., 2006), such as polypropylene (PP) (Kamrannejad et al., 2014), polystyrene (PS) (Shang et al., 2003), and high- (Wang et al., 2015) and low-density polyethylene (PE) films (Thomas et al., 2013; Thomas and Sandhyarani, 2013). TiO_2 nanotubes showed enhanced removal of low-density PE under visible light (Ali et al., 2016), whereas the activity of TiO_2 was improved using copper phthalocyanine (Zhao et al., 2008), polypyrrole (Li et al., 2010), multiwalled carbon nanotubes (An et al., 2014) for PE removal, whereas iron phthalocyanine (Fa et al., 2008) and ferric stearate (Fa et al., 2013) were applied for photodegradable PS. The photocatalytic degradation for dealing with microplastics has not been explored so far.

In this study, we have developed a novel and generalized approach for solid-phase photodegradation of microplastics (PS and PE) and also introduced the effect of different preparation methods on the photocatalytic performance of TiO_2. The degradation mechanism, reaction intermediates, and feasibility of mineralization were investigated. The *in situ* diffuse reflectance infrared Fourier transform spectroscopy (DRIFTS), high-pressure photon ionization (HPPI)-TOFMS, and gas chromatography (GC) spectroscopy results showed that the larger fragments of PS were broken into smaller ones and finally changed into CO_2. Considering the natural availability of TiO_2 and the global environmental impact of microplastics, TiO_2-enhanced photodegradation system may be established into a promising approach to take advantage of natural material for the removal of microplastics. For real application, TiO_2-based films can be fabricated on microplastic filters, which can be directly used for the decomposition of microplastics under UV light irradiation, and it can also avoid the release of toxic intermediates into water in the technologies of liquid phase elimination of microplastics.

RESULTS AND DISCUSSION

Photocatalytic Degradation of PS and PE

The morphological changes in 400-nm PS on TiO_2 nanoparticle films fabricated with water (WT), ethanol (ET), Triton X-100 (TXT), and without catalyst (FTO) before and after UV light irradiation are shown in Figures 1 and S1. It can be seen that PS nanospheres were well dispersed on all films. Figure 1A displays the exact size and morphology of 400-nm PS on FTO (without photocatalyst) at 0 h irradiation. Almost a negligible change in PS size was observed on FTO during the whole photoirradiation reaction (Figure 1B). However, PS spheres exhibited a change in morphology and size on TiO_2-based catalysts at the initial 3 h of photoreaction (Figure S1). The light-induced coalescence of PS during degradation is because the photocatalytic degradation (hydroxyl radical oxidation) at the contact point of packed spheres is slower, which suggests that the degradation takes place on the PS-air interface. A more significant change in PS morphology and size was observed after another 3 and 6 h of irradiation (Figures S1, 1D, 1F, and 1H). TXT film exhibited an obvious change in PS morphology (Figure 1H) and size as compared with ET and WT films. Moreover, we further investigated 700 nm, 1 μm, and 5 μm sized PS spheres on TXT film, which showed significant changes in PS morphology and reduction in sphere size during the photoreaction (Figure S2). The change in PS morphology and size was further analyzed by determining the average diameter, degradation efficiency, and volume change. Based on the above observations, it is reasonable to conclude that TXT is very efficient in the photocatalytic degradation of PS.

Figure 2 displays the PS diameter, degradation efficiency, and inorganic carbon content during the photodegradation reaction. The diameter change of 400-nm PS was almost negligible on FTO, whereas this diameter became 268.18 nm on WT film after 12 h illumination. Simultaneously, the ET and TXT film shows a significant decrease in PS diameter, which was 177.78 and 100.07 nm, respectively (Figure 2A). The difference in photocatalytic performance of films can be ascribed to band energy, surface area, morphology, charge separation, light absorption, and texture (Vahl et al., 2019). Comparing the photocatalytic activity

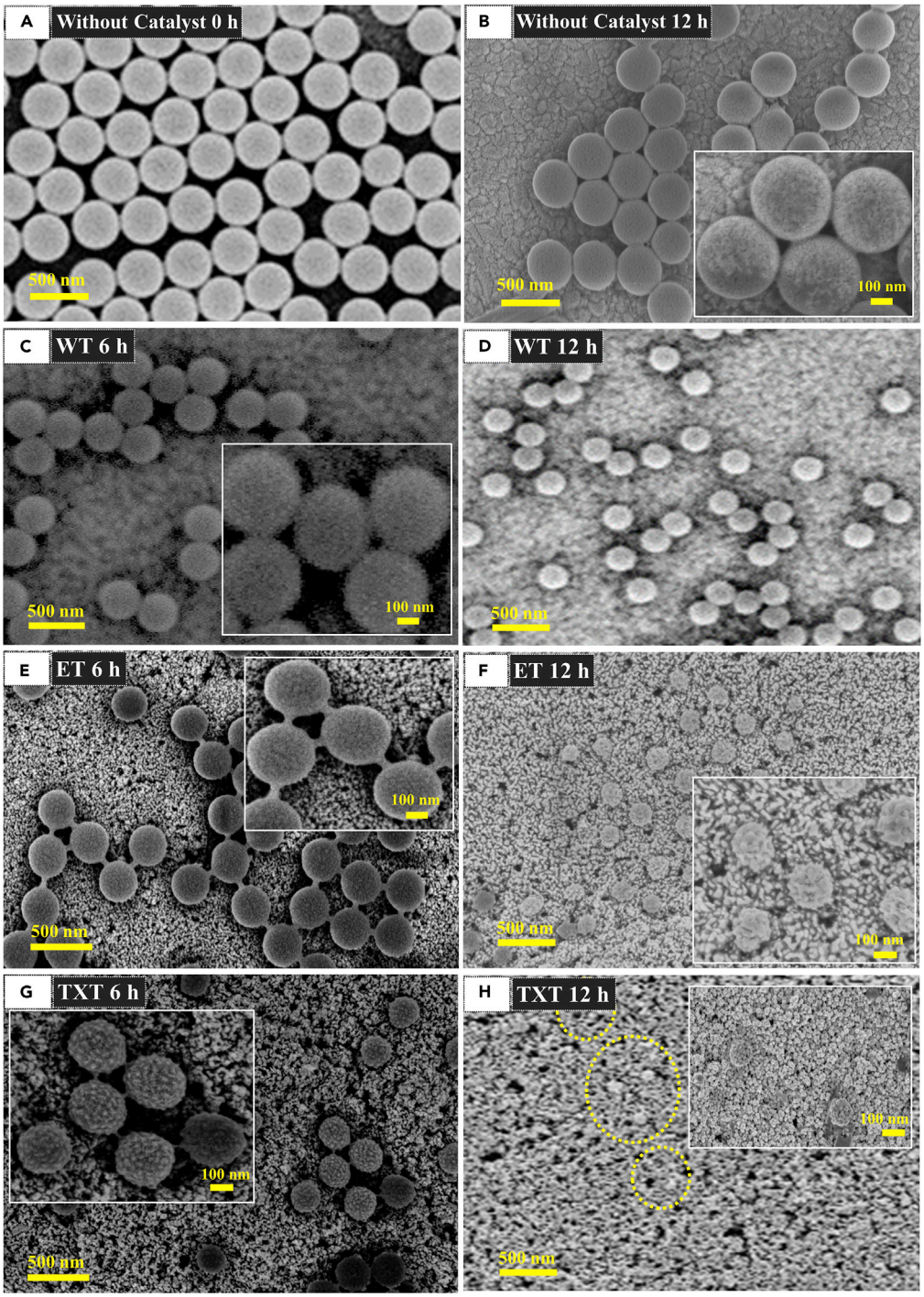

Figure 1. FE-SEM Images of PS Spheres after Different Irradiation Time under 365 nm UV Light

(A) PS spheres on FTO (without catalyst) before irradiation.
(B) Without catalyst after 12 h irradiation.
(C) Water-based TiO_2 (WT) after 6 h irradiation.
(D) WT after 12 h irradiation.
(E) Ethanol-based TiO_2 (ET) after 6 h irradiation.
(F) ET after 12 h irradiation.
(G) Triton X-100 based TiO2 (TXT) after 6 h irradiation.
(H) TXT after 12 h irradiation.

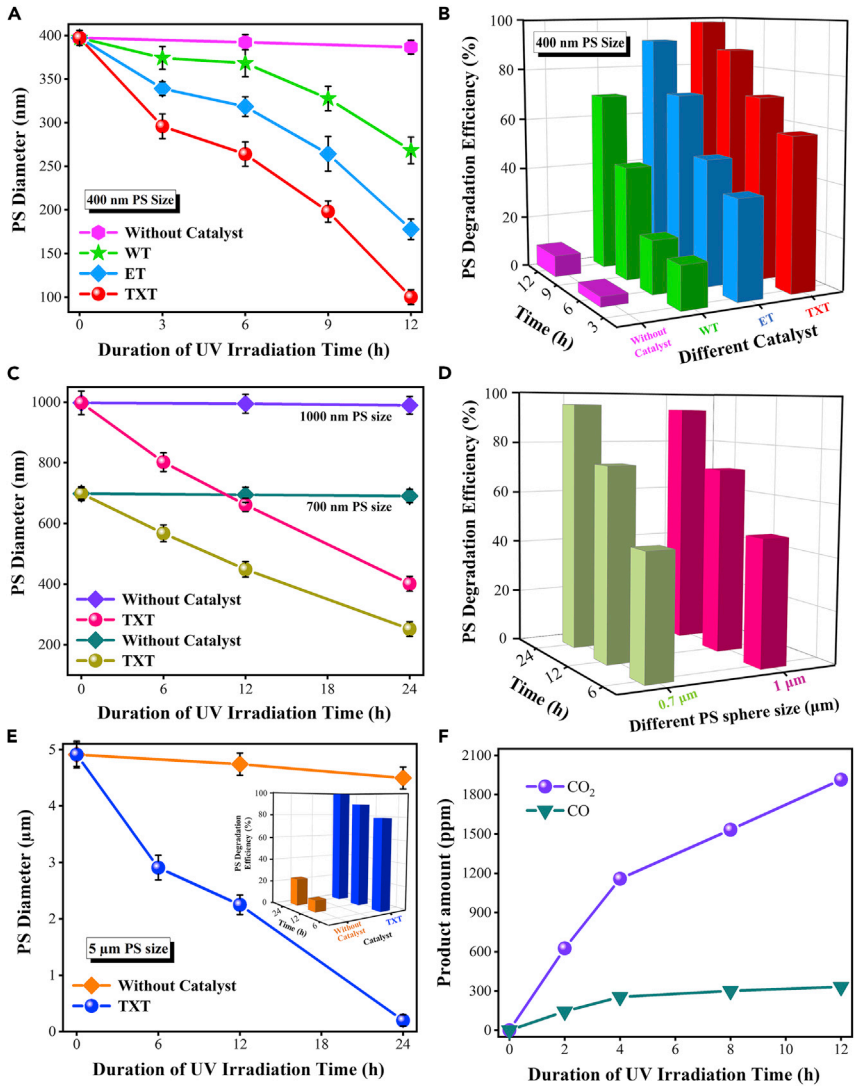

Figure 2. Photocatalytic Degradation of Polystyrene

(A) Diameter change of 400-nm PS on TXT, ET, WT films, and without catalyst under different irradiation time intervals.

(B) PS degradation efficiency (%) with (TXT, ET, WT) and without catalyst.

(C) Diameter change of 1-μm and 700-nm PS on TXT film, and without catalyst.

(D) Degradation efficiency (%) of 1-μm and 700-nm PS on TXT film under 365-nm UV light.

(E) Diameter change of 5-μm PS on TXT film, and without catalyst (inserted degradation efficiency [%] of 5 μm) under 254-nm UV light.

(F) Concentrations of carbon dioxide (CO_2) and carbon monoxide at different stages of photodegradation reaction.

of fabricated films, TXT showed higher performance, which was attributed to its low band energy and good charge separation, which was studied in detail later. Therefore, TXT produces more electron-hole pairs under light irradiation and also extends the charge separation resulting in significant photoactivity for PS removal, whereas the mediocre performance of WT film is presumably due to its large particle size, low surface area, and a poor charge separation ability. The degradation efficiency of PS was calculated by (Equation 1):

$$\text{PS Degradation Efficiency (\%)} = \frac{\text{Initial Volume} - \text{Final Volume}}{\text{Initial Volume}} \times 100 \qquad \text{(Equation 1)}$$

It was observed that the photodegradation of PS increased with increasing irradiation time. After 12 h of UV irradiation, the degradation efficiency of 400-nm PS was 98.40%, 91.04%, and 69.25% for TXT, ET, and WT

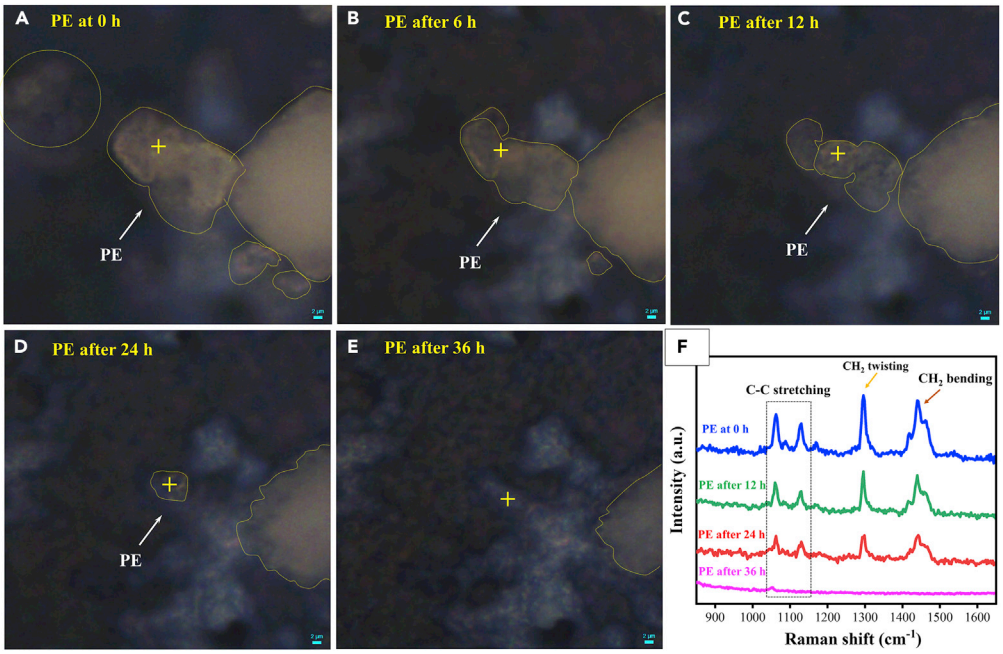

Figure 3. Photocatalytic Degradation of PE on TXT Film under 254-nm UV Light

(A) PE at 0 h; (B) PE after 6 h; (C) PE after 12 h; (D) PE after 24 h; (E) PE after 36 h; (F) Raman spectrum of PE with different time profiles. (Highlighted parts present PE, and the same point was used for Raman imaging and detection throughout the experiment.)

films, respectively (Figure 2B). Since the PS degradation efficiency was negligible on FTO (8.01%), indicating the direct photolysis of PS was insignificant. Figures 2C and 2D present the diameter change and the degradation efficiency of 700-nm and 1-μm PS, which was decreased to 251.96 and 401.28 nm, respectively, after 24 h irradiation. Meanwhile, the degradation efficiency for 1-μm and 700-nm PS was 93.49% and 95.30%, respectively, after 24 h irradiation under 365 nm UV light. However, the degradation efficiency of 5-μm PS was 99.99% after 24 h illumination under 254 nm UV and the faster degradation is attributed to the higher energy of photon and more charge carriers generated (Figure 2E).

Figures S3 and S4 present volume and surface area changes in varying sizes of PS, and effectual changes were observed with the increase in irradiation time. Figures 2F and S3D show the concentration of CO_2 with TiO_2 and PS with TiO_2/PS. At the initial phase, the concentration of CO_2 increases linearly owing to the fast photodegradation of PS (direct contact of PS with TiO_2 nanoparticles) and then slowly decelerates in the subsequent phase because of slow desorption process. CO_2 plot of TiO_2 with PS was 10 times higher than the control experiment signifying that CO_2 was produced from the PS decomposition, whereas in control experiment, a slight quantity of CO_2 might be due to the presence of organic impurities. Moreover, a small amount of carbon monoxide (CO) appeared owing to the stretching of C-H bond in the TiO_2/PS system (Cho and Choi, 2001).

Furthermore, we conducted an experiment to check PS decomposition in the liquid phase to evaluate if it would make the same contribution as the solid phase. The comparison results are illustrated in Figure S5. Interestingly, the mineralization efficiency of microplastic that occurred on the solid (microplastic)-solid (TiO_2) interface was much higher than that in the liquid phase. This is because t there is less chance of hydroxyl radicals and holes to react with microplastic particles in the liquid phase (suspended, close contact between TiO_2 and microplastic particle becomes difficult), whereas on the solid-solid interface the key structural feature is that it facilitates charge separation to hinder recombination and enhances the photocatalytic degradation efficiency (Li and Gray, 2007). Moreover, the exposed surface of PS in the solid phase is higher owing to the direct contact with TiO_2 film, which leads to the direct attack of reactive species without any hindrance, whereas in the liquid phase the slower degradation is due to the hydrophilicity of PS particles in water solution, which makes the attack of reactive species slower.

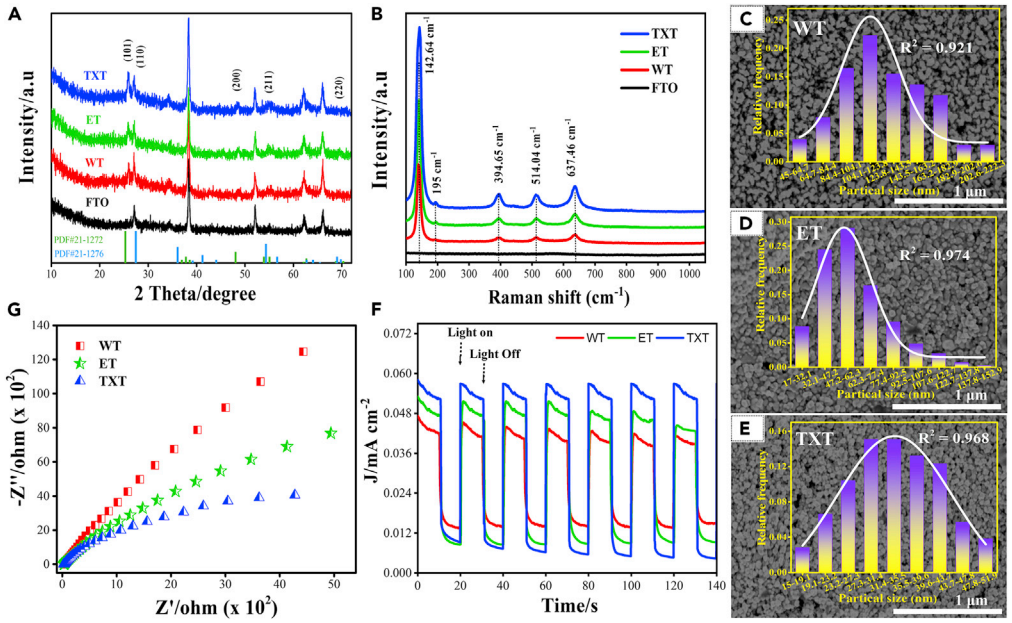

Figure 4. Structure, Morphology, and Optical Properties

(A) XRD patterns of TXT, ET, and WT photocatalysts (XRD pattern of FTO was used as a baseline for comparison with catalyst films).

(B) Raman spectrum of fabricated photocatalyst films.

(C), (D), and (E) FE-SEM images of the nanoporous WT, ET, and TXT photocatalysts with their particle size distribution (inserted).

(F) Amperometric *i-t* curves of TXT, ET, and WT photocatalysts under chopped illumination.

(G) Electrochemical impedance spectroscopy (EIS) Nyquist plot of TXT, ET, and WT catalyst films.

We further investigated the activity of TXT film for the degradation of PE, and analysis was carried out through Raman spectroscopy. Figure 3A presents the actual PE morphology before UV light irradiation, and the plus (+) symbol presents the selected point for Raman detection and spectrum. Interestingly, PE shows changes in morphology and size with the increase in irradiation time (Figures 3B–3D) and finally, tens of micrometers-sized PE particles totally disappeared after 36 h of UV irradiation, signifying the complete degradation of PE (Figure 3E), although an insignificant degradation was observed on FTO (Figure S6). Figure 3F shows the Raman band of PE at 1,064, 1,133, 1,296, and 1,442 cm^{-1}, which corresponds to C-C stretching, CH_2 twisting, and CH_2 bending (Wright et al., 2019). Raman spectra of PE exhibited a decline in PE peak with irradiation time, but no peak of PE was detectable after 36 h of photoreaction, which was consistent with Raman imaging. In summary, TXT film also showed efficient photocatalytic activity for PE degradation under UV light. The oxidation state of TiO_2 film remained the same before and after the degradation reaction, and results are shown in Figure S7. Figure S8 shows the actual morphology of the TXT film before and after the degradation reaction. It can be seen that there was no prominent change in catalyst morphology after 12 h of PS degradation reaction, which suggests that the prepared film is highly stable. We investigated the effect of light energy, wavelength, and degradation rate under different light sources (254 nm, 365 nm, and visible light), and the results are shown in Figure S9.

Structure, Morphology, and Optical Properties of Prepared Catalysts

The crystalline structure of the prepared TiO_2 films on FTO substrate was examined by X-ray diffraction (XRD) as shown in Figure 4A. All diffraction peaks of the synthesized films correspond well to a reference pattern of tetragonal anatase and rutile phases with the joint committee on powder diffraction standards (JCPDS) file Nos. 21-1,272 and 21-1,276. The diffractogram consists of peaks at (2 Theta) 25.28°, 48.04°, and 55.06° along with Miller indices values (101), (200), and (211) of anatase TiO_2, respectively. The peaks at (2 Theta) 27.45° and 36.08° match very well with the diffraction (110) and (101) crystal planes of rutile phase TiO_2. It is notable that the width of (101) planes in TXT was stronger at (2 Theta) 25.28° as compared

with ET and WT representing the higher nano crystallinity of film. The diffraction peaks from FTO glass was also observed, which can be attributed to the thinness and high porosity of TiO_2 films.

Raman spectroscopy is beneficial for local structure analysis of the catalysts. Raman spectrum was recorded at wavenumber 100 to 1,100 cm^{-1}, and the FTO glass spectrum was used as a control experiment. The Raman spectrum of the TiO_2 show peaks at 142.64 (E_g), 195 (E_g), 394.65 (B_{1g}), 514.04 (A_{1g}), and 637.46 cm^{-1} (E_g), which are assigned to the anatase phase of TiO_2, whereas a minor peak that appears at 445 (E_g) is attributed to the rutile phase of TiO_2 (Figure 4B) (Wang et al., 2016). All samples show analogs peak, and no other peak was observed.

The morphology of the prepared TiO_2 films was characterized by using field-emission scanning electron microscopy (FE-SEM) (Figures 4C–4E). Figure 4E revealed that the presence of Triton X-100 significantly affected the morphology of TiO_2 (Suwanchawalit et al., 2017), such as the formation of nanoparticles, induced a particle size reduction, and fine pore formation (Godinez and Darnault, 2011). Particle size can influence the surface area and the recombination rate of photogenerated electron-hole pairs. Organic solvents act as a morphology-directing agent and effect on the texture of film during the annealing process, which leads to change in its optical and electrical properties and pore content. The particle size of the prepared films was calculated by using the nano measurer 1.2 software (inserted in Figures 4C–4E). The average particle size in TXT could be varied between 27.3 and 31.1 nm. However, the average particle size in ET and WT was ranging from 47.2 to 62.3 nm and 104.1 to 123.8 nm, respectively. It could be seen that the distribution curves fit well the Gaussian function with R^2 values of 0.921, 0.974, and 0.968 for WT, ET, and TXT, respectively, indicating that the size distribution of the samples was consistent with a normal distribution. Water contact angle and optical properties measurements of the nanoporous TiO_2 films are shown in Figures S10 and S11, respectively. TEM images of the synthesized film showed that TXT film exhibited cuboid and spherical-shaped particles, whereas ET and WT have only a spherical-shaped particle and a dark color in TEM images was observed owing to a high electron density of Ti element (Figure S12). The cross-sectional SEM images show that TiO_2 film has a thickness of about 1.21 μm (Figure S13). TXT film has a high surface area as compared with ET and WT films, as shown in Figure S14 and Table S1.

The charge carrier generation and separation in the synthesized photocatalysts were investigated by using the amperometric *i-t* technique and electrochemical impedance spectroscopy (EIS) (Figures 4F and 4G). The transient photocurrent response of the films (WT, ET, and TXT) was studied at an applied potential of 0.8 V under simulated solar light illumination. The rise and drop of the photocurrent respond well to chopped light. The photocurrent drops when the light was off and increases instantly when the light was on, specifying that the current was completely due to the light response of the catalyst, and the rate of charge transfer was very speedy. Figure 4F illustrates that the TXT produces the transient photocurrent density of 0.058 mA cm^{-2}, which was higher than the ET (0.053 mA cm^{-2}) and WT (0.046 mA cm^{-2}). This *i-t* result indicates that the TXT has a better efficiency in the generation, separation, and transport of electron-hole pairs, which was in good agreement with the following EIS result. The smaller arc radius suggests a more effective separation of photogenerated electron-hole pairs and faster interfacial charge transfer. As can be seen from Figure 4G, the arc radius of TXT catalyst was smaller than the ET and WT, signifying that TXT could facilitate the effective separation and transfer of photogenerated electron-hole pairs that occur on the TXT surface. These electric characteristics showed that Triton X-100 played an effective role in improving the photocatalytic efficiency of the film.

Mass Spectrum and Degradation Mechanism

Nature of the chemical substances formed during the degradation process of PS was characterized through high-pressure photon ionization (HPPI)-TOFMS. Mass spectra were obtained before and after 120 min of UV irradiation, and no dominant peak was observed at 0 min. Numerous characteristic ion fragments were formed during the photodegradation of PS such as *m/z* = 27 ($C_2H_3^+$), 39 ($C_3H_3^+$), 41 ($C_3H_5^+$), 51 ($C_4H_3^+$), 63 ($C_5H_3^+$), 77 ($C_6H_5^+$), 91 ($C_7H_9^+$), and 105 ($C_8H_9^+$) (Ng et al., 2018). These fragments were originated from the cleavage of PS spheres. The O-containing intermediates were observed with peak *m/z* values 43.01 ($C_2H_3O^+$), 44.94 ($C_2H_5O^+$), 57.03 ($C_3H_5O^+$), 59.04 ($C_3H_7O^+$), and 87.04 ($C_4H_7O_2^+$), but the intensities of these peaks are very weak. Therefore, these peaks were not considered in reaction intermediates. Figure 5A shows the *m/z* spectra of these commonly observed ions. Among the various degradation

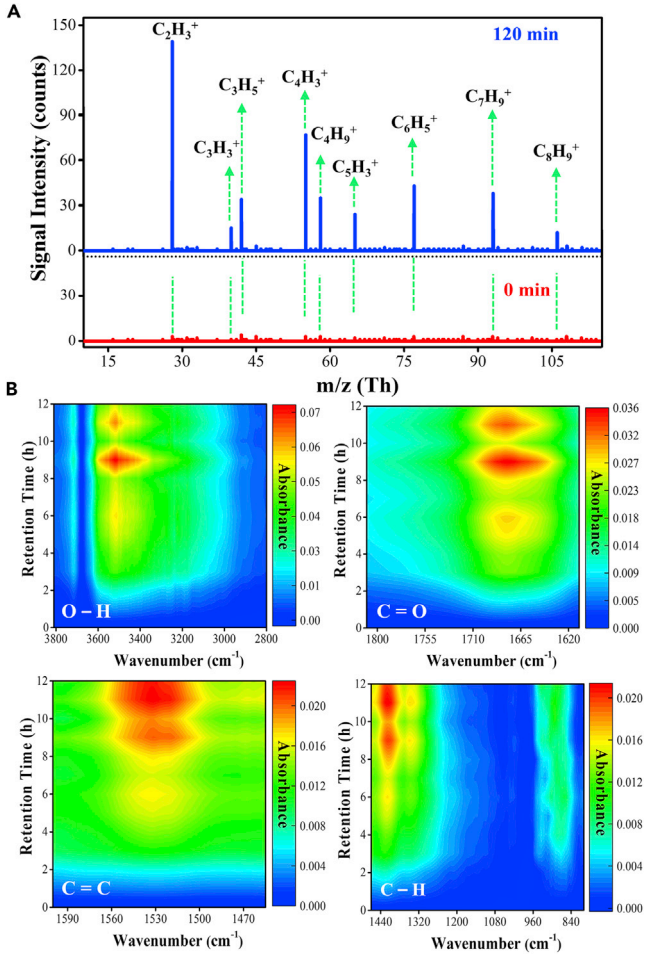

Figure 5. Mass Spectrum and Degradation Mechanism

(A) Mass spectra obtained by high-pressure photon ionization (HPPI)-TOFMS during the photodegradation of PS.

(B) DRIFTS study of PS at different time intervals.

intermediates, the *m/z* 105 belongs to the styrene (Bruns et al., 2017), whereas the *m/z* 77 and 91 corresponds to the benzene and toluene. The other small fragments with *m/z* 27, 39, 41, and 51 were derived due to the breakdown of bigger *m/z* fragments. As the photodegradation reaction proceeds, the PS fragments were further broken and finally changed into CO_2 according to the GC result.

For further consolidation, an *in situ* DRIFTS study was done to understand the chemical functionality of organic species during the photodegradation reaction of PS (Figures 5B and S15). The IR spectra of TiO_2/PS at about 3,600–3,200 cm^{-1} were attributed to the hydroxyl group formation (Kaczmarek et al., 2008), and the band that appears at 1,650–1700 cm^{-1} was due to a carbonyl group (C=O) (Subramani and Sepperumal, 2016; Zan et al., 2004). These two bands were assigned to the formation of aromatic and aliphatic ketones of the acetophenone and OH group in the PS chain. The reason for these two bands formation may be the chain scission or a competitive cross-linking or the oxidation of the benzene ring. A minor peak at 2,314 cm^{-1} was observed, which was due to CO_2 formation during the reaction. The band at 1,527 cm^{-1} was associated with stretching of the C=C bonds (Gipson et al., 2015) from the aromatic ring, and the intensity of these bands increases continuously with increasing the illumination time of TiO_2/PS composite. The band that appears at 1,425 cm^{-1} was due to C-H bend (Truc et al., 2017), whereas the band at 873 cm^{-1} corresponds to C-H stretching vibration of the aromatic ring and deformation vibration in cyclic carbonyl compounds (Al-Kadhemy et al., 2016). The bond smashing provides evidence that the TiO_2 and UV irradiation accelerate the bond cleavage of PS. Figure S16 presents the thermogravimetric analysis (TGA) curve of PS, which signifies the complete mineralization after 24 h irradiation.

In order to understand the photodegradation mechanism of PS, including the role, and possible pathway for the formation of active species, corresponding effective scavengers were added in the reaction system. Figure S17 shows the change in PS diameter over TXT film after 6 h irradiation under different reaction conditions. TBA was employed to scavenge the $^{\bullet}OH$ (hydroxyl radical), EDTA to trap h^+ (holes), and the anaerobic experiment was conducted to check the role of oxygen. The addition of EDTA completely inhibited the PS degradation, whereas TBA and anaerobic experiments induced the depression effect. A slight degradation in anaerobic condition was observed owing to the attack of electron on PS particles yielding the PS cation radical, which further leads to its degradation (Lu et al., 2011; Szabó-Bárdos et al., 2011). Along this, holes and hydroxyl radicals were also formed by TiO_2 and became dominant oxidants to attack plastic particles that cause degradation (Lee et al., 2014). Therefore, we conclude that h^+, $^{\bullet}OH$, and oxygen play an important role in the photodegradation of PS, whereas the h^+ was the dominant active species in our reaction. The possible reaction of h^+ with other species produces more active species causing the highly favorable generation of ^{i}OH. Moreover, the degradation performance of microplastics as compared with the literature and details are presented in Table S2.

The photodegradation reaction of PS on a solid state was initiated by holes and reactive oxidative species such as $\bullet OH$ and $O_2^{\bullet -}$. UV light stimulates the TiO_2 to produce an electron in the conduction (e^-_{CB}) and formation of a positive hole in the valence band (h^+_{VB}) (Equation 2). There are two possibilities for reaction initiation. In the first pathway, the oxidation reaction takes place at the valence band. h^+_{VB} is a powerful oxidizing agent and capable of oxidizing organic compounds resulting in CO_2 and H_2O (Equation 3), as well as it can also oxidize the compounds by generating hydroxyl radicals (Equation 4) (Kesselman et al., 1997). $\bullet OH$ radicals have an electrophilic nature; they can nonselectively oxidize all electron-rich organic compounds and eventually result in their mineralization (Equation 5) (Shang et al., 2003).

$$TiO_2 \xrightarrow{hv} h^+_{VB} + e^-_{CB} \quad \text{(Equation 2)}$$

$$h^+_{VB} + \text{microplastic} \rightarrow CO_2 + H_2O \quad \text{(Equation 3)}$$

$$h^+_{VB} + H_2O \rightarrow {}^{\bullet}OH + H^+ \quad \text{(Equation 4)}$$

$$^{\bullet}OH + \text{microplastic} \rightarrow CO_2 + H_2O \quad \text{(Equation 5)}$$

n the second pathway, the degradation reaction takes place at the conduction band. The e^-_{CB} reacts with oxygen, forming a superoxide radical (Equation 6). This superoxide radical reaction with water produces $^{\bullet}OOH$ (Equation 7) that generates hydrogen peroxide (Equation 8). The hydrogen peroxide finally changed into $^{\bullet}OH$ (Equation 9), which reacts with microplastic and leads to its degradation (Cho and Choi, 2001).

$$O_2 + e^-_{CB} \rightarrow O_2^{\bullet -} \quad \text{(Equation 6)}$$

$$O_2^{\bullet -} + H_2O \rightarrow {}^{\bullet}OOH + OH^- \quad \text{(Equation 7)}$$

$$2\,{}^{\bullet}OOH \rightarrow O_2 + H_2O_2 \quad \text{(Equation 8)}$$

$$H_2O_2 \rightarrow 2\,{}^{\bullet}OH \quad \text{(Equation 9)}$$

Conclusion

This work proposed the efficient degradation and complete mineralization of microplastics by TiO_2 nanoparticles film under UV light irradiation. Among synthesized films, TXT exhibits high performance as compared with ET and WT. A significant photocatalytic degradation and mineralization for varying sizes of PS such as 5 μm, 1 μm, and 700 nm and polyethylene (PE) were observed by TXT. The superior activity of TXT film is due to surface hydrophilicity and film texture. Surface hydrophilicity can enhance the interaction between semiconductors and plastic, particles that improved the film texture leading to charge transfer and separation that results in the fast degradation of microplastics. The degradation mechanism was studied by *in situ* DRIFTS and mass spectrometer, showing the generation of hydroxyl, carbonyl, and carbon-hydrogen groups, which is evidence for the photodegradation of PS. The film fabrication process does not include any costly, toxic, and hazardous chemicals, which makes this method highly efficient, beneficial, and economically important. Moreover, the solid phase photodegradation of microplastics also avoids the release of possible toxic intermediates into water in the liquid phase technology. Overall, the present study put forward a green and sustainable method for microplastic waste degradation from the environment.

Limitations of the Study

The main limitation of this study is that, initially, microplastics should be separated from water bodies, which can be done by using microplastic filters. Second, the complete mineralization of microplastics was observed under UV light. So, there is need for promising applications for microplastic mineralization under visible light.

Resource Availability

Lead Contact

Further information and requests for resources and reagents should be directed to and will be fulfilled by the Lead Contact, Zhang Liwu (zhanglw@fudan.edu.cn).

Materials Availability

This study did not generate new materials. Detailed information on experiments can be found in the accompanying Transparent Methods.

Data and Code Availability

This study did not generate a new code. All relevant data are available from the Lead Contact upon reasonable request.

METHODS

All methods can be found in the accompanying Transparent Methods supplemental file.

SUPPLEMENTAL INFORMATION

Supplemental Information can be found online at https://doi.org/10.1016/j.isci.2020.101326.

ACKNOWLEDGMENTS

The authors gratefully acknowledge financial support from National Natural Science Foundation of China (Nos. 21677037, 21976030, 21507011and 21607027), the Ministry of Science and Technology of the People's Republic of China (2016YFE0112200), and the Natural Science Foundation of Shanghai (Nos. 19ZR1471200 and 17ZR1440200).

AUTHOR CONTRIBUTIONS

L.Z. was the originator of the concept and planned and supervised the experiments. I.N. synthesized the photocatalysts, analyzed data, carried out photodegradation experiments, and wrote the manuscript. A.-U.-R.B., K.L., and H.C. performed the PEC experiments. T.W. and Y.L. did the *in situ* DRIFTS and HPPI-TOFMS measurements. S.A. and Y.Y. carried out the GC analysis. Y.F. assisted in Raman experiments. All authors reviewed the manuscript.

DECLARATION OF INTERESTS

The authors declare no competing financial interests.

Received: April 10, 2020
Revised: June 11, 2020
Accepted: June 26, 2020
Published: July 24, 2020

REFERENCES

Al-Kadhemy, M.F.H., Rasheed, Z.S., and Salim, S.R. (2016). Fourier transform infrared spectroscopy for irradiation coumarin doped polystyrene polymer films by alpha ray. J. Radiat. Res. Appl. Sci. *9*, 321–331.

Ali, S.S., Qazi, I.A., Arshad, M., Khan, Z., Voice, T.C., and Mehmood, C.T. (2016). Photocatalytic degradation of low density polyethylene (LDPE) films using titania nanotubes. Environ. Nanotechnol. Monit. Manag. *5*, 44–53.

An, Y., Hou, J., Liu, Z., and Peng, B. (2014). Enhanced solid-phase photocatalytic degradation of polyethylene by TiO_2–MWCNTs nanocomposites. Mater. Chem. Phys. *148*, 387–394.

Andrady, A.L. (2011). Microplastics in the marine environment. Mar. Pollut. Bull. *62*, 1596–1605.

Barboza, L.G.A., Vethaak, A.D., Lavorante, B.R., Lundebye, A.-K., and Guilhermino, L. (2018). Marine microplastic debris: an emerging issue for food security, food safety and human health. Mar. Pollut. Bull. *133*, 336–348.

Besseling, E., Wegner, A., Foekema, E.M., Van Den Heuvel-Greve, M.J., and Koelmans, A.A. (2012). Effects of microplastic on fitness and PCB bioaccumulation by the lugworm *Arenicola marina* (L.). Environ. Sci. Technol. *47*, 593–600.

Bruns, E.A., Slowik, J.G., Haddad, I.E., Kilic, D., Klein, F., Dommen, J., Temime-Roussel, B., Marchand, N., Baltensperger, U., and Prévôt, A.S. (2017). Characterization of gas-phase organics using proton transfer reaction time-of-flight mass spectrometry: fresh and aged residential wood combustion emissions. Atmos. Chem. Phys. *17*, 705–720.

Cho, S., and Choi, W. (2001). Solid-phase photocatalytic degradation of PVC–TiO_2 polymer composites. J. Photoch. Photobio. A Chem. *143*, 221–228.

Fa, W., Guo, L., Wang, J., Guo, R., Zheng, Z., and Yang, F. (2013). Solid-phase photocatalytic degradation of polystyrene with TiO_2/Fe $(St)_3$ as catalyst. J. Appl. Polym. Sci. *128*, 2618–2622.

Fa, W., Zan, L., Gong, C., Zhong, J., and Deng, K. (2008). Solid-phase photocatalytic degradation of polystyrene with TiO_2 modified by iron (II) phthalocyanine. Appl. Catal. B Environ. *79*, 216–223.

Feng, H.-M., Zheng, J.-C., Lei, N.-Y., Yu, L., Kong, K.H.-K., Yu, H.-Q., Lau, T.-C., and Lam, M.H. (2010). Photoassisted Fenton degradation of polystyrene. Environ. Sci. Technol. *45*, 744–750.

Fossi, M.C., Coppola, D., Baini, M., Giannetti, M., Guerranti, C., Marsili, L., Panti, C., de Sabata, E., and Clò, S. (2014). Large filter feeding marine organisms as indicators of microplastic in the pelagic environment: the case studies of the Mediterranean basking shark (*Cetorhinus maximus*) and fin whale (*Balaenoptera physalus*). Mar. Environ. Res. *100*, 17–24.

Garcia, J.M., and Robertson, M.L. (2017). The future of plastics recycling. Science *358*, 870–872.

Gipson, K., Stevens, K., Brown, P., and Ballato, J. (2015). Infrared spectroscopic characterization of Photoluminescent polymer nanocomposites. J. Spectrosc. *2015*, 1–9.

Godinez, I.G., and Darnault, C.J. (2011). Aggregation and transport of nano-TiO_2 in saturated porous media: effects of pH, surfactants and flow velocity. Water Res. *45*, 839–851.

Inkinen, S., Hakkarainen, M., Albertsson, A.-C., and Södergård, A. (2011). From lactic acid to poly (lactic acid) (PLA): characterization and analysis of PLA and its precursors. Biomacromolecules *12*, 523–532.

Jakubowicz, I. (2003). Evaluation of degradability of biodegradable polyethylene (PE). Polym. Degrad. Stab. *80*, 39–43.

Kaczmarek, H., Felczak, A., and Szalla, A. (2008). Studies of photochemical transformations in polystyrene and styrene-maleic anhydride copolymer. Polym. Degrad. Stab. *93*, 1259–1266.

Kamrannejad, M.M., Hasanzadeh, A., Nosoudi, N., Mai, L., and Babaluo, A.A. (2014). Photocatalytic degradation of polypropylene/TiO_2 nano-composites. Mater. Res. *17*, 1039–1046.

Kang, J., Zhou, L., Duan, X., Sun, H., Ao, Z., and Wang, S. (2019). Degradation of cosmetic microplastics via functionalized carbon nanosprings. Matter *1*, 745–758.

Kemp, T.J., and McIntyre, R.A. (2006). Influence of transition metal-doped titanium (IV) dioxide on the photodegradation of polystyrene. Polym. Degrad. Stab. *91*, 3010–3019.

Kesselman, J.M., Weres, O., Lewis, N.S., and Hoffmann, M.R. (1997). Electrochemical production of hydroxyl radical at polycrystalline Nb-doped TiO_2 electrodes and estimation of the partitioning between hydroxyl radical and direct hole oxidation pathways. J. Phys. Chem. B *101*, 2637–2643.

Klavarioti, M., Mantzavinos, D., and Kassinos, D. (2009). Removal of residual pharmaceuticals from aqueous systems by advanced oxidation processes. Environ. Int. *35*, 402–417.

Koelmans, A.A., Besseling, E., and Shim, W.J. (2015). Nanoplastics in the Aquatic Environment. Critical Review, Marine Anthropogenic Litter (Springer), pp. 325–340.

Lee, W.-L.W., Lu, C.-S., Lin, H.-P., Chen, J.-Y., and Chen, C.-C. (2014). Photocatalytic degradation of ethyl violet dye mediated by TiO_2 under an anaerobic condition. J. Taiwan Inst. Chem. Eng. *45*, 2469–2479.

Li, A., Zhu, W., Li, C., Wang, T., and Gong, J. (2019). Rational design of yolk–shell nanostructures for photocatalysis. Chem. Soc. Rev. *48*, 1874–1907.

Li, G., and Gray, K.A. (2007). The solid-solid interface: explaining the high and unique photocatalytic reactivity of TiO_2-based nanocomposite materials. Chem. Phys. *339*, 173–187.

Li, J., Liu, H., and Chen, J.P. (2018). Microplastics in freshwater systems: a review on occurrence, environmental effects, and methods for microplastics detection. Water Res. *137*, 362–374.

Li, S., Xu, S., He, L., Xu, F., Wang, Y., and Zhang, L. (2010). Photocatalytic degradation of polyethylene plastic with polypyrrole/TiO_2 nanocomposite as photocatalyst. Polym. Plast. Technol. Eng. *49*, 400–406.

Lu, S.-y., Wu, D., Wang, Q.-l., Yan, J., Buekens, A.G., and Cen, K.-F.J.C. (2011). Photocatalytic decomposition on nano-TiO_2: destruction of chloroaromatic compounds. Chemosphere *82*, 1215–1224.

MacArthur, E. (2017). Beyond plastic waste. Science *358*, 843.

McCormick, A., Hoellein, T.J., Mason, S.A., Schluep, J., and Kelly, J.J. (2014). Microplastic is an abundant and distinct microbial habitat in an urban river. Environ. Sci. Technol. *48*, 11863–11871.

Moore, C.J. (2008). Synthetic polymers in the marine environment: a rapidly increasing, long-term threat. Environ. Res. *108*, 131–139.

Ng, K.M., Lau, Y.T.R., Weng, L.T., Yeung, K.L., and Chan, C.M. (2018). ToF-SIMS and computation analysis: fragmentation mechanisms of polystyrene, polystyrene-d_5, and polypentafluorostyrene. Surf. Interface Anal. *50*, 220–233.

Rochman, C.M., Regan, F., and Thompson, R.C. (2017). On the harmonization of methods for measuring the occurrence, fate and effects of microplastics. Anal. Methods *9*, 1324–1325.

Shang, J., Chai, M., and Zhu, Y. (2003). Photocatalytic degradation of polystyrene plastic under fluorescent light. Environ. Sci. Technol. *37*, 4494–4499.

Subramani, M., and Sepperumal, U. (2016). FTIR analysis of bacterial mediated chemical changes in Polystyrene foam. Ann. Biol. Res. *7*, 55–61.

Suwanchawalit, C., Buddee, S., and Wongnawa, S. (2017). Triton X-100 induced cuboid-like $BiVO_4$ microsphere with high photocatalytic performance. J. Environ. Sci. *55*, 257–265.

Szabó-Bárdos, E., Somogyi, K., Törő, N., Kiss, G., and Horváth, A.J.A.C.B.E. (2011). Photocatalytic decomposition of l-phenylalanine over TiO_2: identification of intermediates and the mechanism of photodegradation. Appl. Catal. B Environ. *101*, 471–478.

Thomas, R.T., Nair, V., and Sandhyarani, N. (2013). TiO_2 nanoparticle assisted solid phase photocatalytic degradation of polythene film: a mechanistic investigation. Colloids Surf. A. Physicochem. Eng. Asp. *422*, 1–9.

Thomas, R.T., and Sandhyarani, N. (2013). Enhancement in the photocatalytic degradation of low density polyethylene–TiO_2 nanocomposite films under solar irradiation. RSC Adv. *3*, 14080–14087.

Truc, N.T.T., Lee, C.-H., Lee, B.-K., and Mallampati, S.R. (2017). Development of hydrophobicity and selective separation of hazardous chlorinated plastics by mild heat treatment after PAC coating and froth flotation. J. Hazard. Mater. *321*, 193–202.

Vahl, A., Veziroglu, S., Henkel, B., Strunskus, T., Polonskyi, O., Aktas, O.C., and Faupel, F. (2019). Pathways to tailor photocatalytic performance of TiO_2 thin films deposited by reactive magnetron sputtering. J. Mater. *12*, 2840.

van Weert, S., Redondo-Hasselerharm, P.E., Diepens, N.J., and Koelmans, A.A. (2019). Effects of nanoplastics and microplastics on the growth of sediment-rooted macrophytes. Sci. Total Environ. *654*, 1040–1047.

Wang, S., Zhang, J., Liu, L., Yang, F., and Zhang, Y. (2015). Evaluation of cooling property of high density polyethylene (HDPE)/titanium dioxide (TiO_2) composites after accelerated ultraviolet (UV) irradiation. Sol. Energy Mater. Sol. Cells *143*, 120–127.

Wang, W.-K., Chen, J.-J., Zhang, X., Huang, Y.-X., Li, W.-W., and Yu, H.-Q. (2016). Self-induced synthesis of phase-junction TiO_2 with a tailored rutile to anatase ratio below phase transition temperature. Sci. Rep. *6*, 20491.

Watts, A.J., Lewis, C., Goodhead, R.M., Beckett, S.J., Moger, J., Tyler, C.R., and Galloway, T.S. (2014). Uptake and retention of microplastics by the shore crab Carcinus maenas. Environ. Sci. Technol. *48*, 8823–8830.

Wright, S.L., Levermore, J.M., and Kelly, F.J. (2019). Raman spectral imaging for the detection of inhalable microplastics in ambient particulate matter samples. Environ. Sci. Technol. *53*, 8947–8956.

Yang, Y., Yang, J., Wu, W.-M., Zhao, J., Song, Y., Gao, L., Yang, R., and Jiang, L. (2015). Biodegradation and mineralization of polystyrene by plastic-eating mealworms: part 2. Role of gut microorganisms. Environ. Sci. Technol. *49*, 12087–12093.

Yuan, K., Cao, Q., Lu, H.-L., Zhong, M., Zheng, X., Chen, H.-Y., Wang, T., Delaunay, J.-J., Luo, W., and Zhang, L. (2017). Oxygen-deficient WO_{3-x}@ TiO_{2-x} core–shell nanosheets for efficient photoelectrochemical oxidation of neutral water solutions. J. Mater. Chem. A *5*, 14697–14706.

Zan, L., Tian, L., Liu, Z., and Peng, Z. (2004). A new polystyrene–TiO_2 nanocomposite film and its photocatalytic degradation. Appl. Catal. A Gen. *264*, 237–242.

Zan, L., Wang, S., Fa, W., Hu, Y., Tian, L., and Deng, K. (2006). Solid-phase photocatalytic degradation of polystyrene with modified nano-TiO_2 catalyst. Polymer *47*, 8155–8162.

Zhao, X., Li, Z., Chen, Y., Shi, L., and Zhu, Y. (2008). Enhancement of photocatalytic degradation of polyethylene plastic with CuPc modified TiO_2 photocatalyst under solar light irradiation. Appl. Surf. Sci. *254*, 1825–1829.

Zhou, L., Wang, L., Zhang, J., Lei, J., and Liu, Y. (2016). Well-dispersed Fe_2O_3 nanoparticles on g-C_3N_4 for efficient and stable photo-fenton photocatalysis under visible-light irradiation. Eur. J. Inorg. Chem. *34*, 5387–5392.

iScience, Volume *23*

Supplemental Information

Complete Photocatalytic Mineralization of Microplastic on TiO_2 Nanoparticle Film

Iqra Nabi, Aziz-Ur-Rahim Bacha, Kejian Li, Hanyun Cheng, Tao Wang, Yangyang Liu, Saira Ajmal, Yang Yang, Yiqing Feng, and Liwu Zhang

Supplemental Information for

Complete Photocatalytic Mineralization of Microplastic on TiO_2 Nanoparticle Film

Iqra Nabi[1], Aziz-Ur-Rahim Bacha[1], Kejian Li[1], Hanyun Cheng[1], Tao Wang[1], Yangyang Liu[1], Saira Ajmal[1], Yang Yang[1], Yiqing Feng[1], and Liwu Zhang[1, 2]*

[1]Shanghai Key Laboratory of Atmospheric Particle Pollution and Prevention, Department of Environmental Science & Engineering, Fudan University, Shanghai, 200433, Peoples' Republic of China

[2]Shanghai Institute of Pollution Control and Ecological Security, Shanghai, 200092, Peoples' Republic of China

*Corresponding Author:

E-mail: zhanglw@fudan.edu.cn ; Phone/Fax: +86-21-6564-2781

Table of contents:

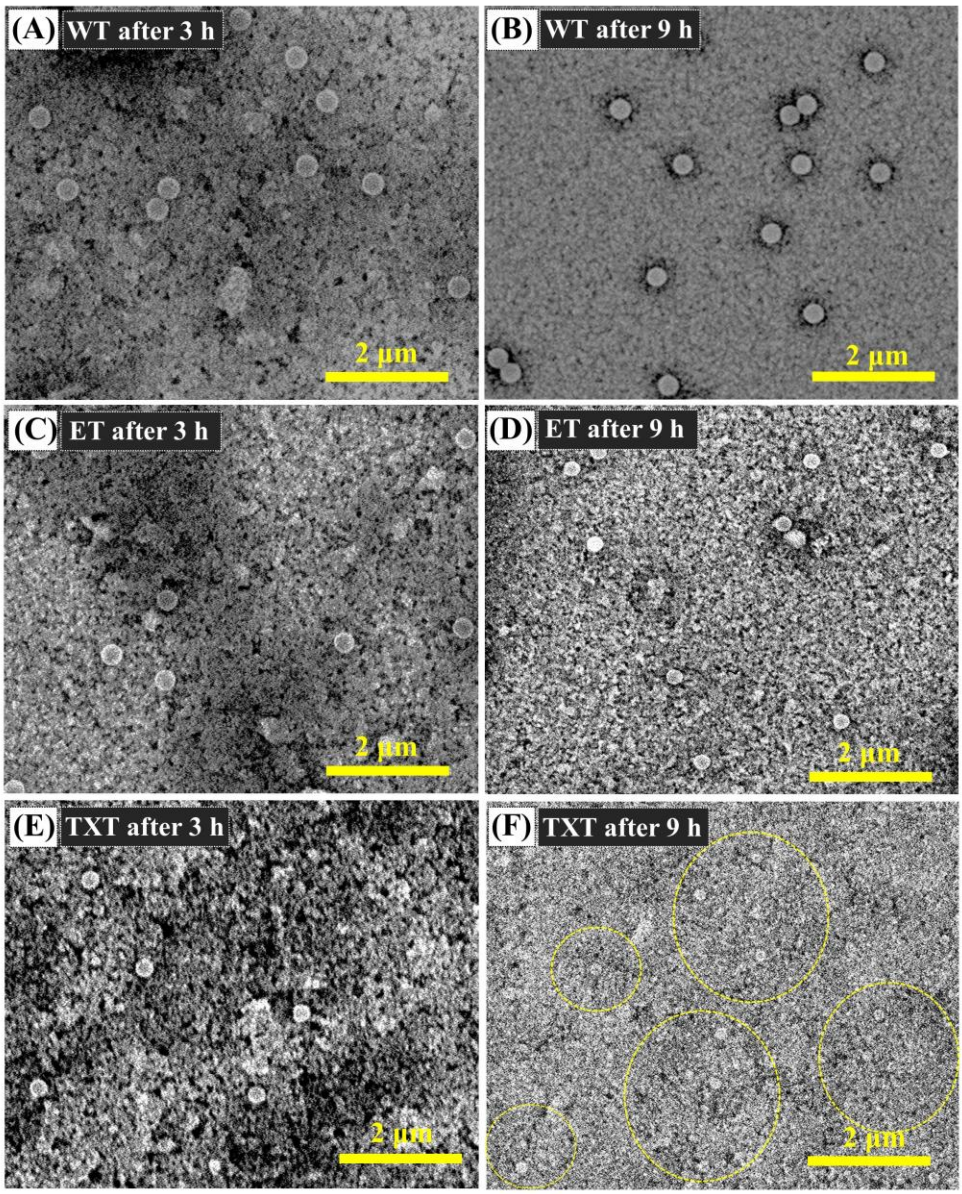

Figure S1. SEM images of 400 nm PS on TiO_2 based catalysts under 365 nm UV light. Related to Figure 1. (A, B) WT after 3 and 9 h irradiation **(C, D)** ET after 3 and 9 h irradiation and **(E, F)** TXT after 3 and 9 h irradiation. (SEM images were taken through phenom Prox).

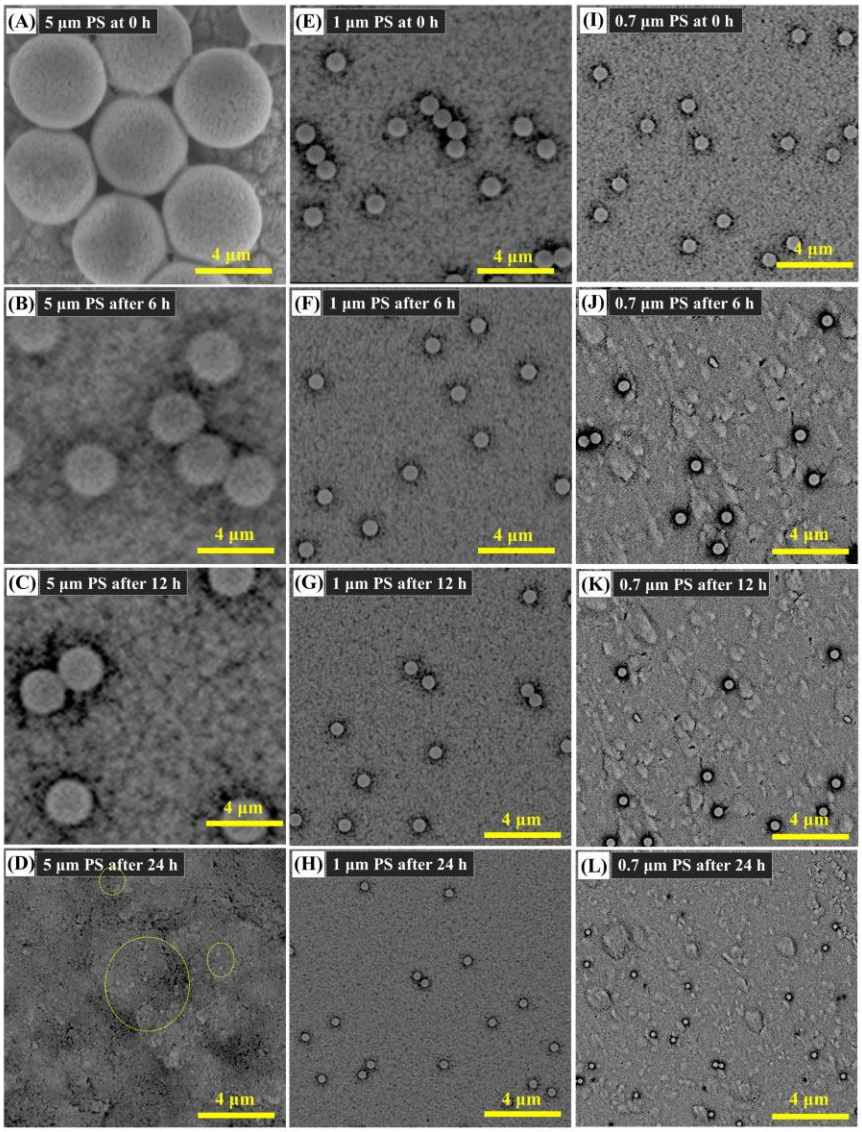

Figure S2. SEM images of 5 µm, 1 µm and 700 nm PS on TXT film. Related to Figure 2. (A) 5 µm PS at 0 h of UV irradiation **(B)** 5 µm PS at 6 h of UV irradiation **(C)** 5 µm PS at 12 h of UV irradiation **(D)** 5 µm PS at 24 h of UV irradiation **(E)** 1 µm at 0 h of UV irradiation **(F)** 1 µm at 6 h of UV irradiation **(G)** 1 µm at 12 h of UV irradiation **(H)** 1 µm at 12 h of UV irradiation **(I)** 700 nm PS at 0 h of UV irradiation **(J)** 700 nm PS at 6 h of UV irradiation **(K)** 700 nm PS at 12 h of UV irradiation **(L)** 700 nm PS at 24 h of UV irradiation. (SEM images were taken through phenom Prox and 5 µm PS degradation experiment was carried out through 254 nm UV light while other experiments (1 µm and 700 nm**)** was done under 365 nm UV light).

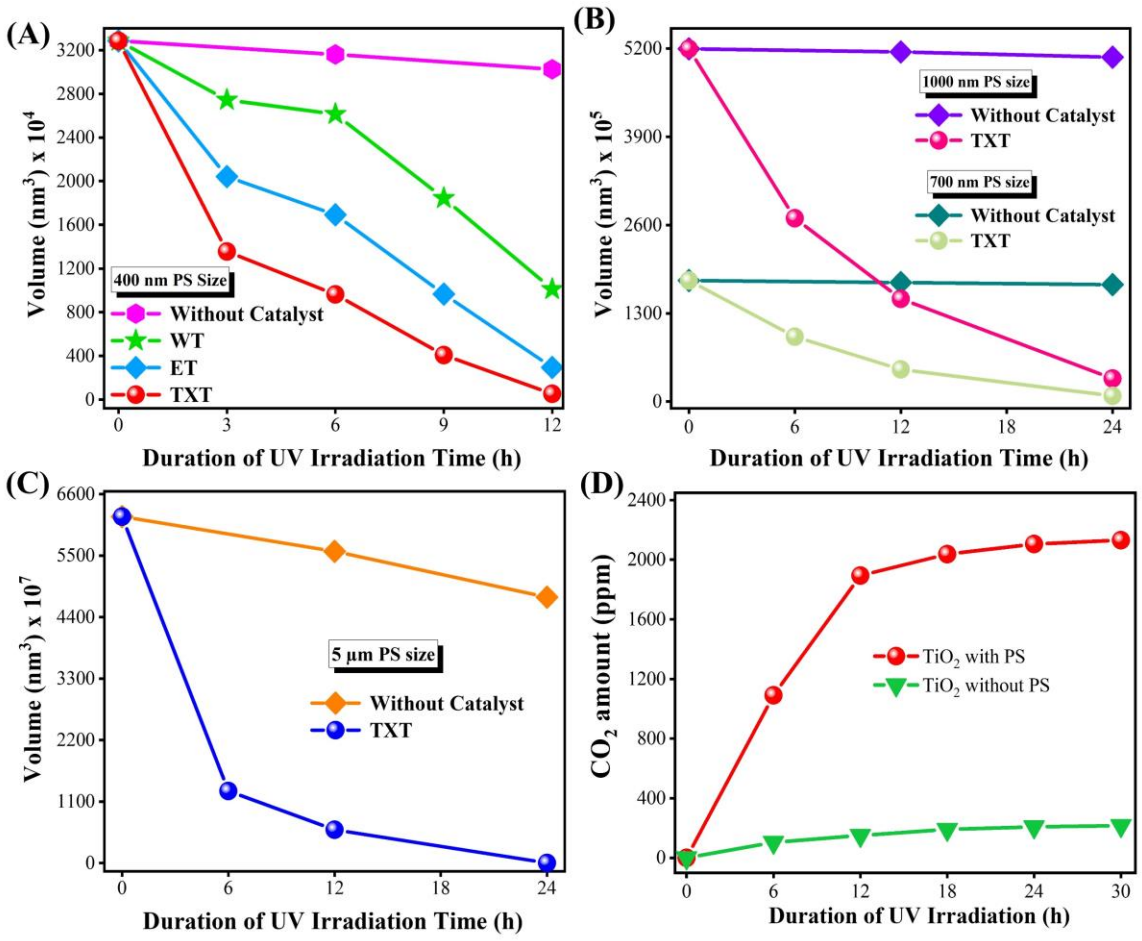

Figure S3. Volume changes of varying size PS and CO_2 concentration. Related to Figure 2. (A) 400 nm PS on WT, ET, and TXT film under 365 nm UV light. **(B)** Volume change of 1 µm and 700 nm PS by TXT film under 365 nm UV light. **(C)** 5 µm PS volume change by TXT film under 254 nm UV light. **(D)** CO_2 concentrations in TiO_2 with and without PS at different stages of photodegradation reaction.

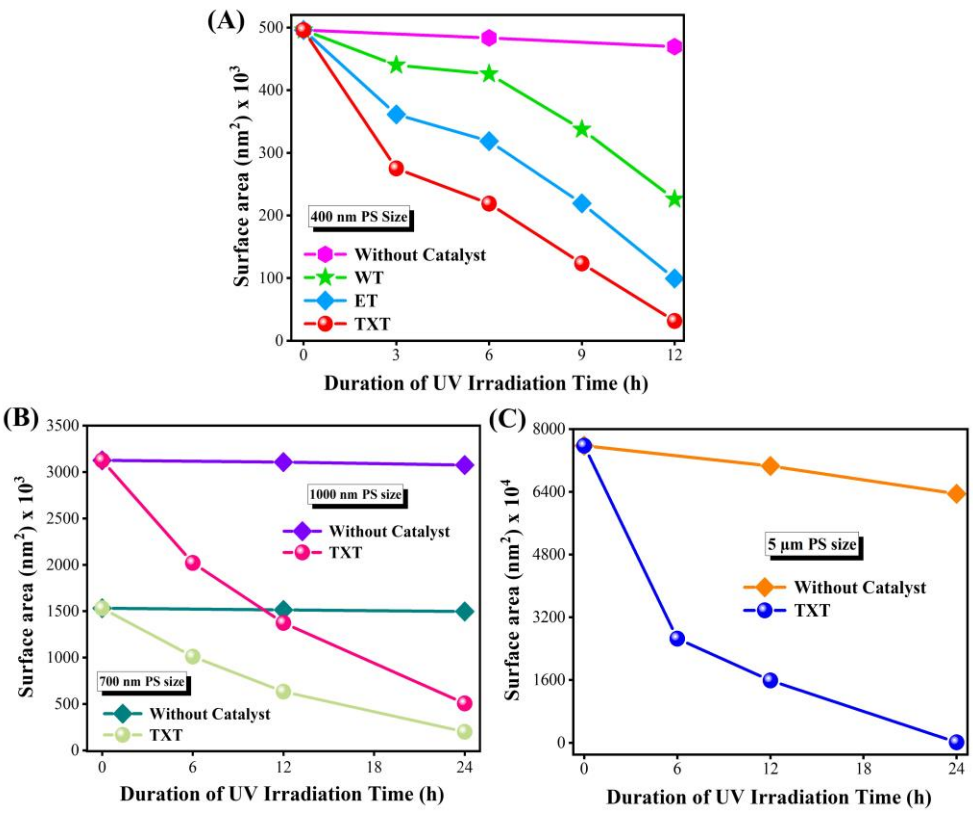

Figure S4. Surface area changes in varying size PS. Related to Figure 2. (A) 400 nm PS on WT, ET, and TXT film under 365 nm UV light. **(B)** Surface area change of 1 µm and 700 nm PS by TXT film under 365 nm UV light. **(C)** 5 µm PS surface area change by TXT film under 254 nm UV light. (Figure S4A-C displays the prominent changes in surface area of varying sizes of PS against different times under UV light irradiation. Surface area changes in 400 nm PS on FTO (without photocatalysts) were negligible, while an effective change was observed on TXT, ET, and WT films (Figure S4A). Additionally, by comparing the surface area changes of PS on fabricated films, TXT showed higher performance, which was due to its unique properties such as bandgap, crystal shape, charge separation, etc. Figure S4B suggests that the surface area in 700 nm PS and 1 µm PS were also changed with the increase in irradiation time. Moreover, a significant change in surface area was observed in 5 µm PS (Figure S4C). Notably, the surface area of varying sizes of PS was decreased with the increase in irradiation time).

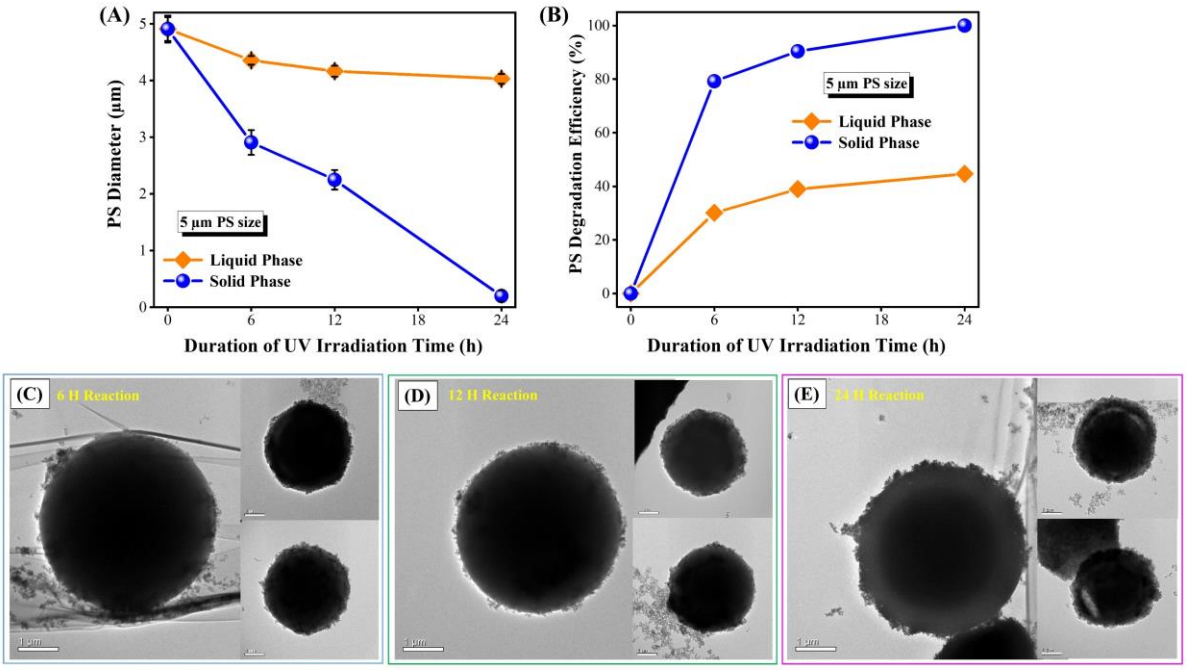

Figure S5. Solid-phase vs. liquid-phase degradation of 5 μm PS under 254 nm UV light with different irradiation time interval. Related to Figure 2. (A) Diameter change of 5 μm PS **(B)** Degradation efficiency (%) of 5 μm PS **(C)** TEM images of 5 μm PS spheres in liquid phase after 6 h reaction. **(D)** TEM images of 5 μm PS spheres in the liquid phase after 12 h reaction. **(E)** TEM images of 5 μm PS spheres in the liquid phase after 24 h reaction. The experiment was carried out at its natural pH.

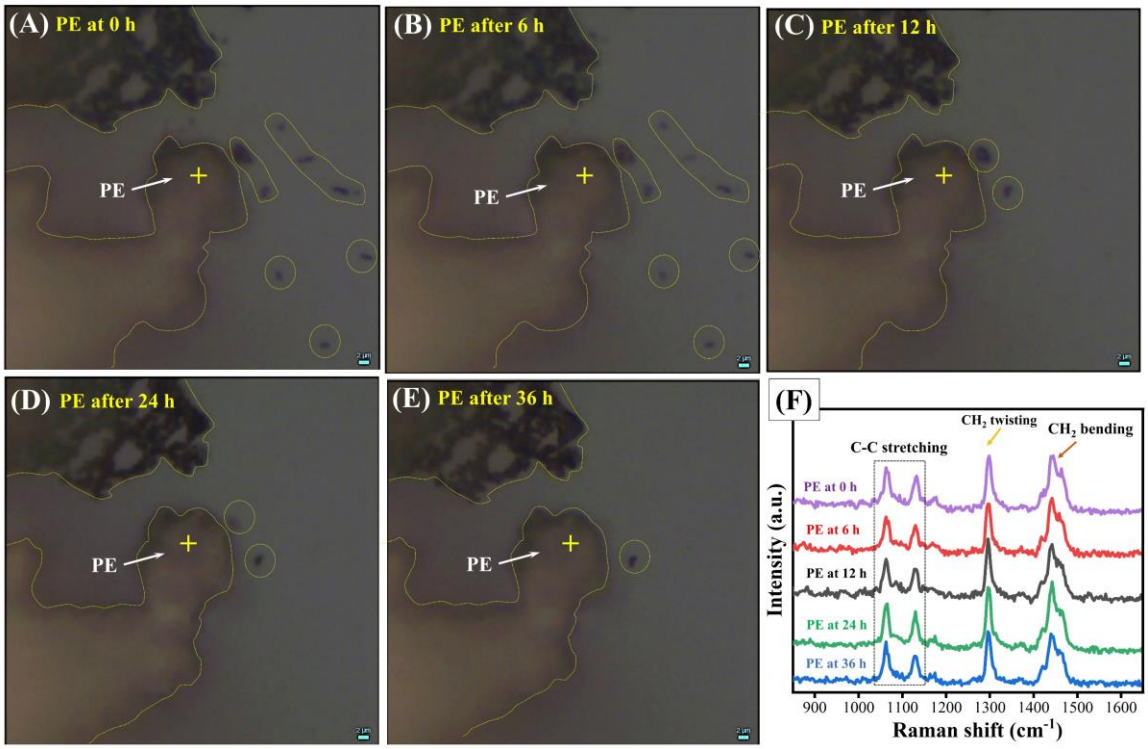

Figure S6. Photocatalytic degradation of PE on FTO (without catalyst) under 254 nm UV light. Related to Figure 3. (A) PE at 0 h **(B)** PE after 6 h **(C)** PE after 12 h **(D)** PE after 24 h **(E)** PE after 36 h **(F)** RAMAN spectrum of PE with different time profiles. (Highlighted parts present PE, and the same point was used for Raman imaging and detection throughout the experiment).

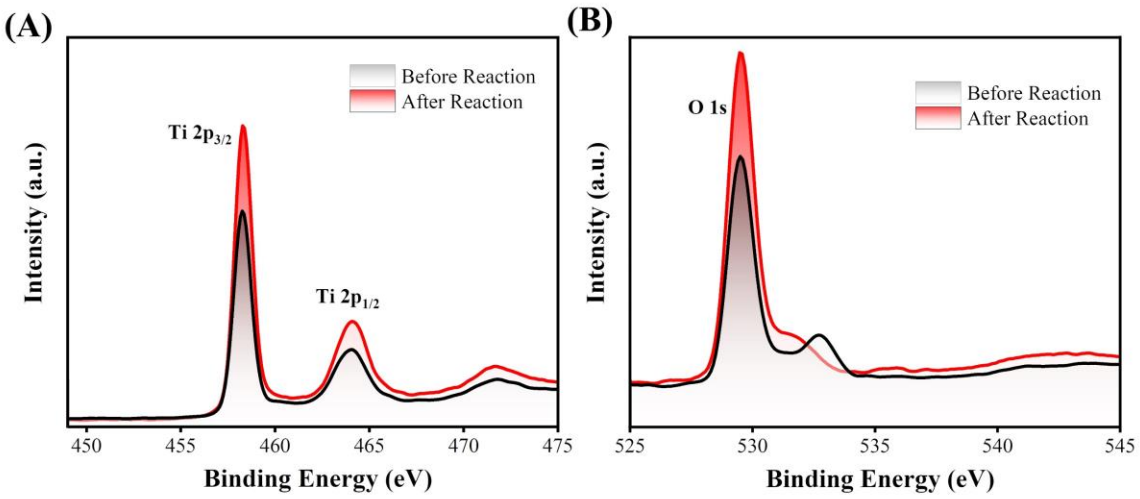

Figure S7. X-ray photoelectron spectra of TXT film before and after the reaction. Related to Figure 2-3. (A) Ti 2p **(B)** O1s. (X-ray photoelectron spectroscopy (XPS) analysis was performed to determine the oxidation state of TiO_2 film before and after the degradation experiment. Figure S7A displays the spectra of Ti 2p, in which two peaks were detected at 458.38 and 464.08 eV, corresponding to the binding energy of Ti $2p_{3/2}$ and Ti $2p_{1/2}$ due to the presence of Ti $^{4+}$ state. Figure S7B presents the spectra of O 1s spectra, in which binding energy of the O 1s was observed at 532.18 eV due to the presence O^{2-} in TiO_2 lattice. After reaction, the increase in binding energy was due to the oxidation of PS particles).

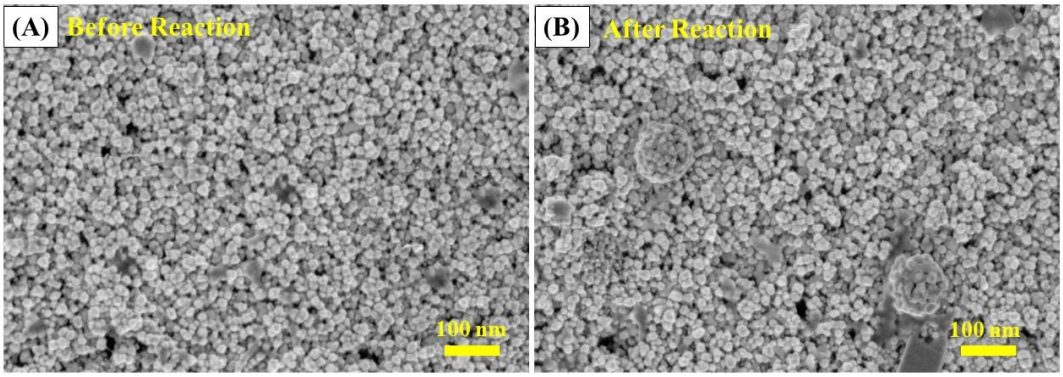

Figure S8. Morphological analysis of TiO_2 films (TXT)) before and after 12 h reaction. Related to Figure 2-3.

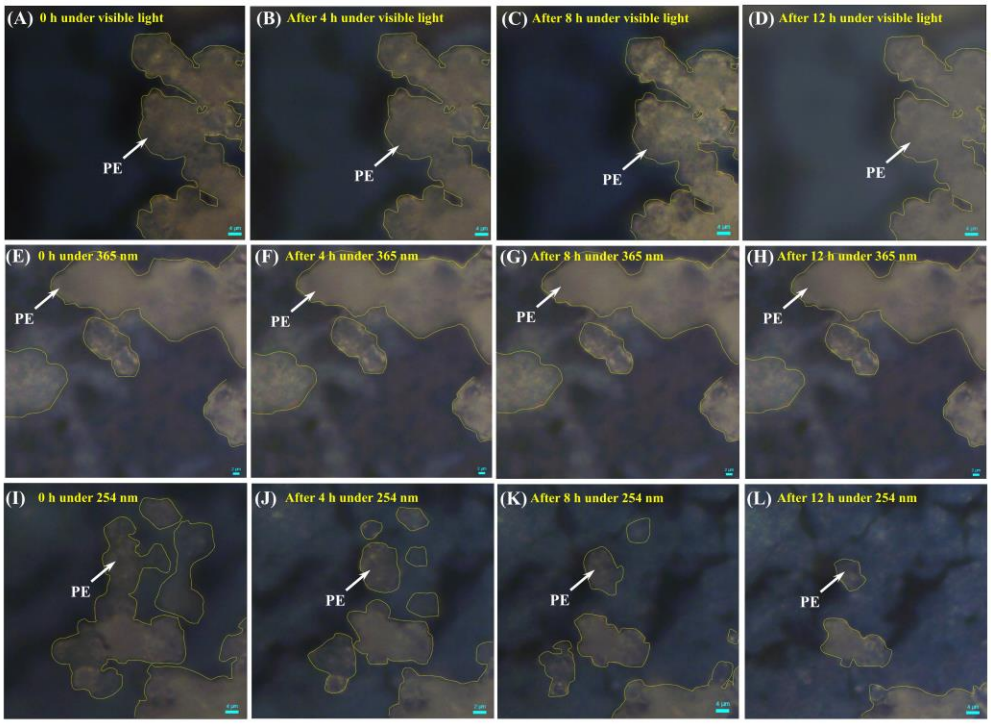

Figure S9. Photocatalytic degradation of PE on TiO_2 film under different irradiation sources. Related to Figure 3. (A-D) PE degradation under visible light **(E-H)** PE degradation under 365 nm UV light **(I-L)** PE degradation under 254 nm UV light. (Highlighted parts present PE). Photodegradation of microplastic depends on various parameters such as the size of microplastic, concentration of microplastic quantity, catalyst amount, light intensity, irradiation time, surface area, and light absorbance of catalyst. Figure S9 shows the degradation of PE under different light sources. It can be seen that the PE degradation was insignificant under visible and 365 nm UV light. A significant change in PE degradation was observed under 254 nm UV light due to its short wavelength and strong energy, which leads to the fast generation of free radicals in the plastic matrix, preferring radical's combination comparative to reaction with oxygen (Shyichuk and White, 2000). The UV light has a particular impact on the degradation of polymers, especially in the range from 290-400 nm, while the influence of visible light was negligible (Decker and Mayo, 1973). The outcomes of this result suggested that 254 nm UV light is more powerful for the degradation of microplastics.

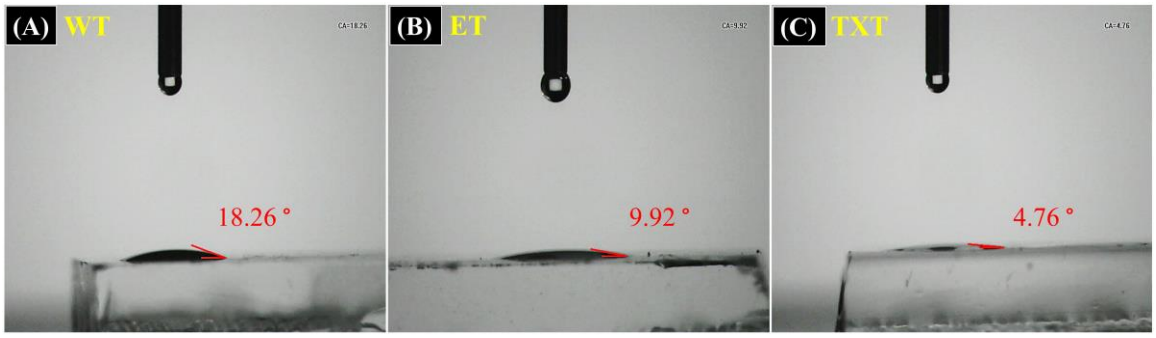

Figure S10. Hydrophilicity Measurement. Related to Figure 4. The water contact angle of **(A) WT, (B) ET, and (C) TXT (Sessile water drops on fabricated films).** Water contact angle measurement is the most common method for determining the surface hydrophilicity changes in films (WT, ET, and TXT), as presented in Figure S10. Basically, the wettability of a material is directly proportional to the surface tension of the liquid and inversely proportional to the contact angle and pore size of the material. The application of a surfactant not only reduces the surface tension of liquid but also causes a decrease in contact angle. It has been observed that the ET and WT films have a contact angle of 9.92° and 18.26°, which were higher as compared to that of TXT. The smaller contact angle value (4.76°) of TXT representing that the Triton X-100 not only improves the wettability but also smooth the film.

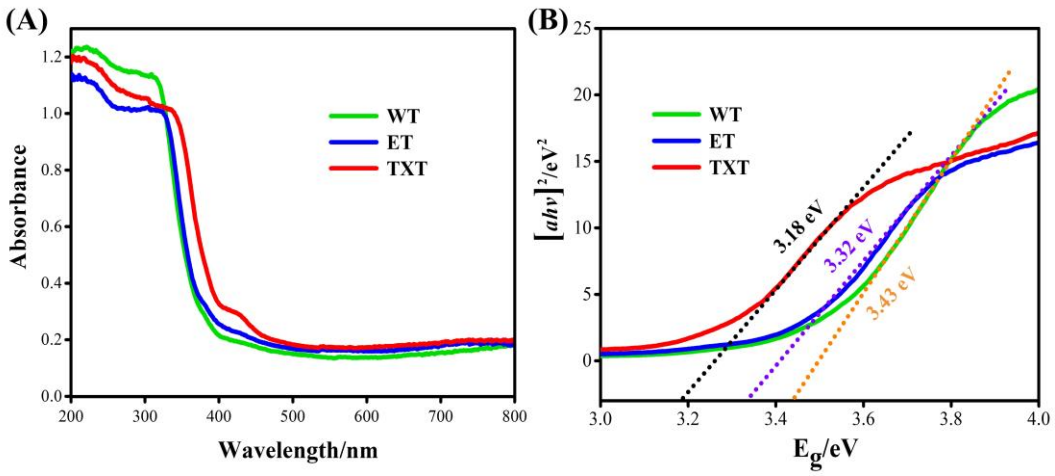

Figure S11. Optical Measurements. Related to Figure 4. (A) UV–vis absorption spectrum of TXT, ET, and WT **(B)** The Tauc plot of the TXT, ET, and WT nanoporous film. (UV–vis diffraction reflection spectroscopy (UV–vis DRS shows the absorption edges at about 390 nm representing the strong UV absorption region of WT and ET, while in TXT, a noticeable shift in the absorption edge towards the visible region at wavelength > 400 nm was observed (Figure S11A). The shift in the visible region has been claimed as a consequence of exciton confinement with a decrease in particle size indicative of the quantum size effect (Satoh et al., 2008). The bandgap of a semiconductor photocatalyst is linked with its absorption wavelength, and the bandgap decreases with an increasing absorption edge (Karthiga et al., 2015). The bandgap value of TXT, ET, and WT catalysts are 3.18, 3.32, and 3.43 eV, respectively (Figure S11B). The result confirms that triton X-100 based TiO_2 can efficiently improve the light absorption).

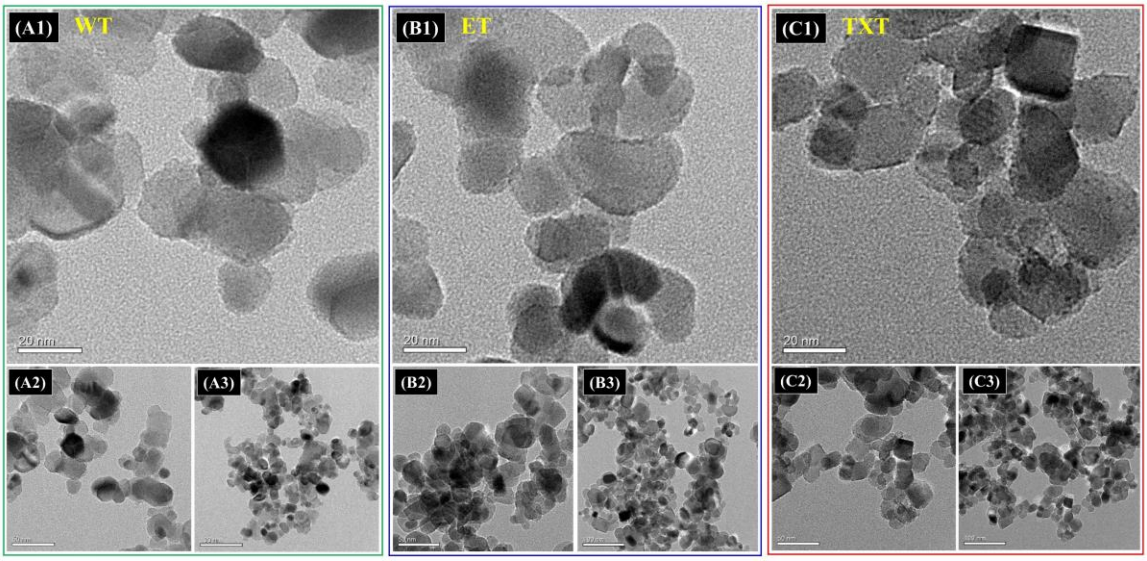

Figure S12. TEM images of TiO_2 films with 20 nm, 50 nm, and 100 nm scale bars. Related to Figure 4. (A1-A3) WT film. **(B1-B3)** ET film. **(C1-C3)** TXT film.

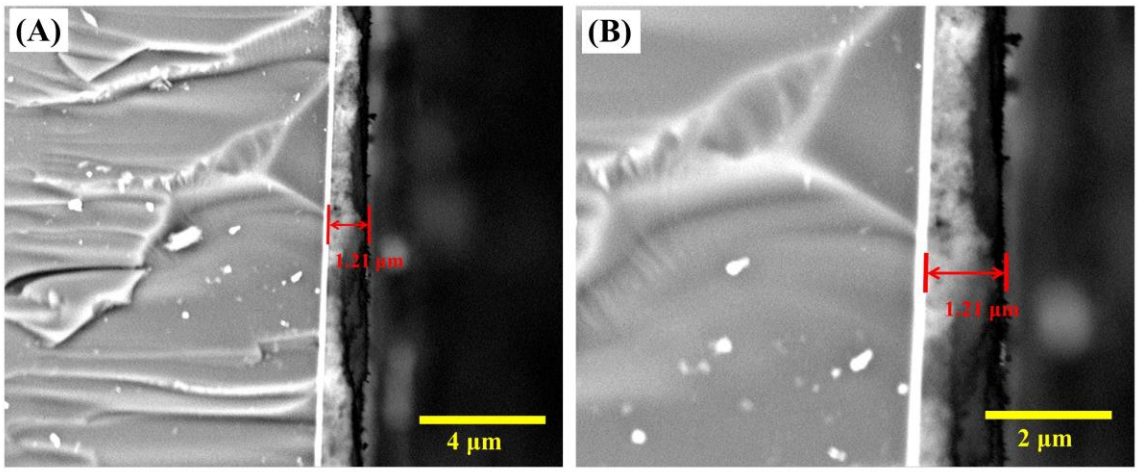

Figure S13. The cross-sectional SEM images of TiO_2 nanoparticles film. Related to Figure 4.

(A) TXT film at 4 µm scale bars. **(B)** TXT film at 2 µm scale bars.

Table S1. BET surface area, pore-volume, and pore size of the prepared catalysts. Related to Figure 4, S14.

Sample	BET surface area (m^2/g)	Pore volume (cm^3/g)	Pore size (nm)
WT	50.65	0.329	21.50
ET	53.13	0.357	21.19
TXT	55.74	0.390	34.69

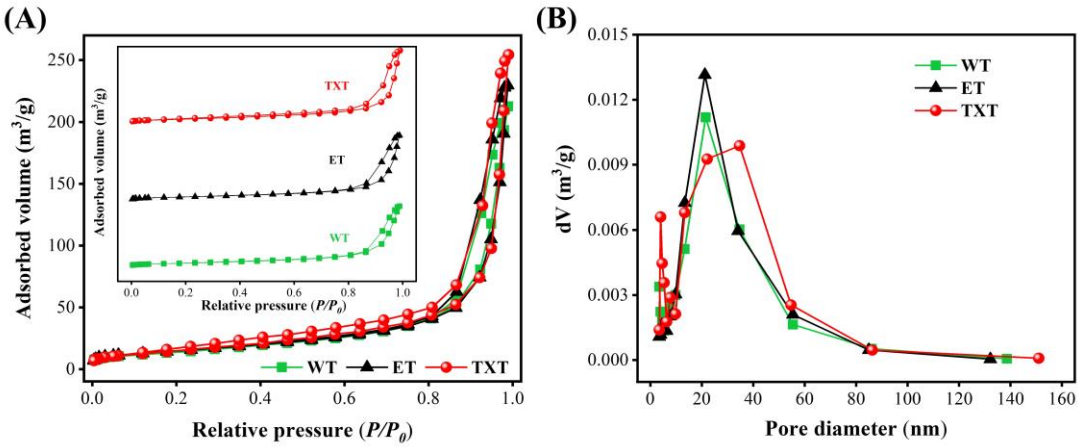

Figure S14. Nitrogen isotherm and pore diameter distribution of TiO_2 films. Related to Figure 4. (A) Nitrogen isotherm of TXT, ET, and WT **(B)** Pore diameter distribution curve of TXT, ET, and WT. (Specific surface area and pore-size distribution analysis of prepared TiO_2 films were measured through Brunauer-Emmett-Teller (BET). Table S1 shows the BET results of TXT, ET, and WT films which were calculated by using the multipoint BET method. It was interesting to observe that TXT film has a high surface area, pore-volume, and pore size as compared to ET and WT films. It can be seen in Figure S14A, all TiO_2 films show the type H3 accordance with BDDT classification presenting the existence of mesopores. Figure S14B shows that the pore diameter of TXT film was higher as compared to the ET and WT films).

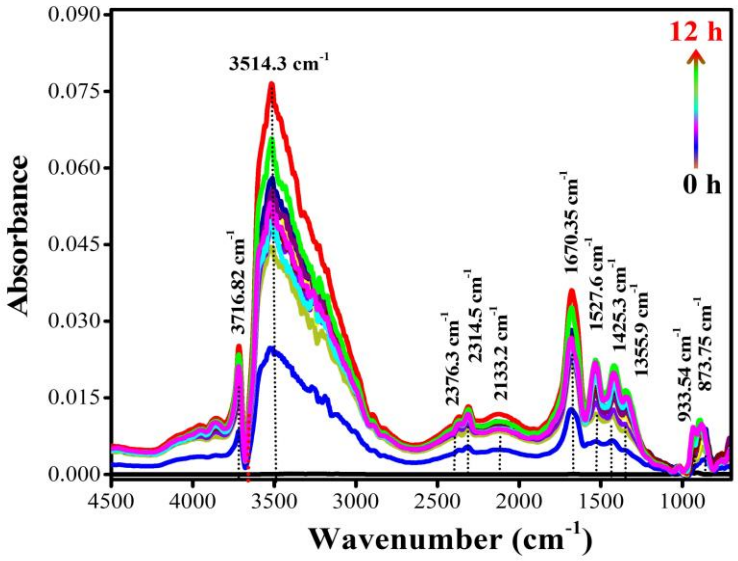

Figure S15. *In-situ* DRIFTs spectrum of PS with a time interval. Related to Figure 5.

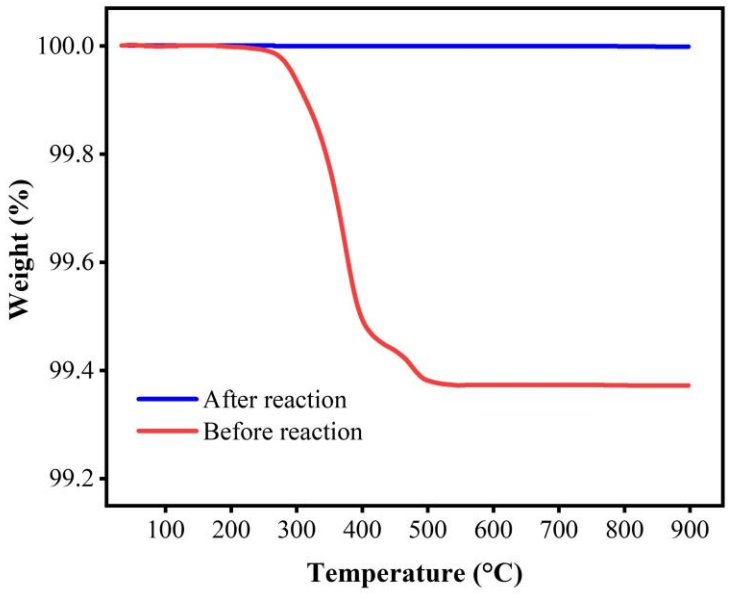

Figure S16. Mineralization of PS. Related to Figure 2. Thermogravimetric analysis of polystyrene loaded TiO_2 film before and after UV irradiation. (The complete mineralization was examined through thermogravimetric analysis (TGA), and the curves are presented in Figure S16. TGA of polystyrene (PS) loaded TiO_2 film showed different weight loss percentages at different temperatures before and after UV irradiation. Before reaction, thermal decomposition of polystyrene began at 263 °C, and a sudden decrease in weight was noticed at a narrow temperature range from 234-274 °C accompanied with a shoulder peak at about 280 °C. The complete decomposition of PS was taken place at 490 °C and then directly changed to gaseous species. Interestingly, negligible change in the TGA curve was observed after the degradation reaction, signifying the complete mineralization of PS and stability of the TiO_2 sample).

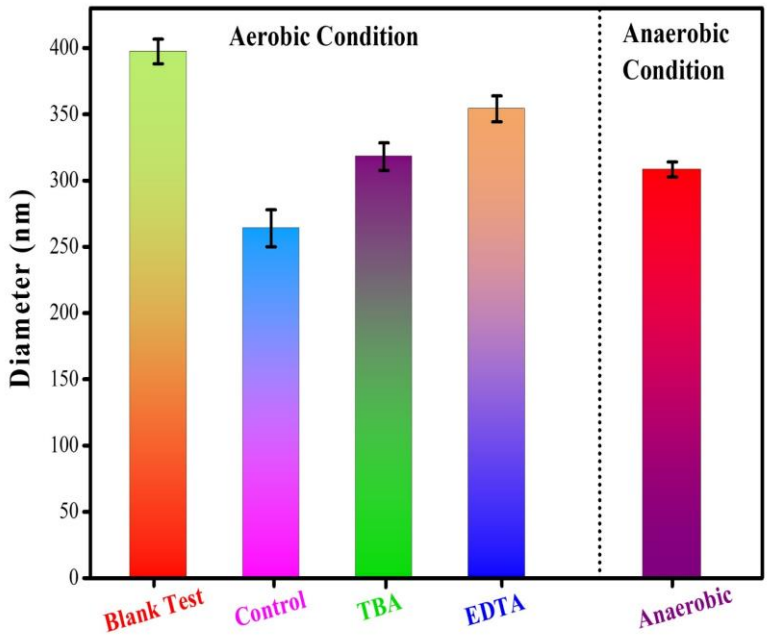

Figure S17. Detection of active species. Related to Figure 5. Hole Scavenging experiment result after 6 h of photoirradiation (Blank test was conducted without a photocatalyst (PS was dropped on cleaned FTO) control experiment was done on TXT film, 10 mM EDTA and 1000 mM TBA was added in 2 mL PS solution and 30 µL PS was dropped on TXT film for active species detection).

Table S2. Microplastics degradation reported by various studies. Related to Figure 2.

Catalysts	Morphology	Microplastics Type	Degradation System	Degradation Efficiency	Light Source	Reference
PE/N-TiO_2	Powder	HDPE	Liquid	6.40 % after 20 h	Fluorescent visible light	(Ariza-Tarazona et al., 2019)
C, N-TiO_2	Powder	HDPE	Liquid	71.77 % after 50 h	LED lamp with visible spectrum	(Ariza-Tarazona et al., 2020)
Mn@NCNTs	Powder	PE	Liquid	54 % after 8 h	0.2 g/L; PMS at 160℃	(Kang et al., 2019)
Photooxid-ation	-	^{14}C-PS	Liquid	28.1 % after 48 h	254 nm UV light	(Tian et al., 2019)
TiO_2	Film	PS	Solid	99.99 % after 24 h	254 nm UV light	This study
TiO_2	Powder	PS	Liquid	44.66 % after 12 h	254 nm UV light	This study

Here, HDPE = High-density polyethylene; PE = Polyethylene; ^{14}C-PS = Adioactively polystyrene, PS = Polystyrene.

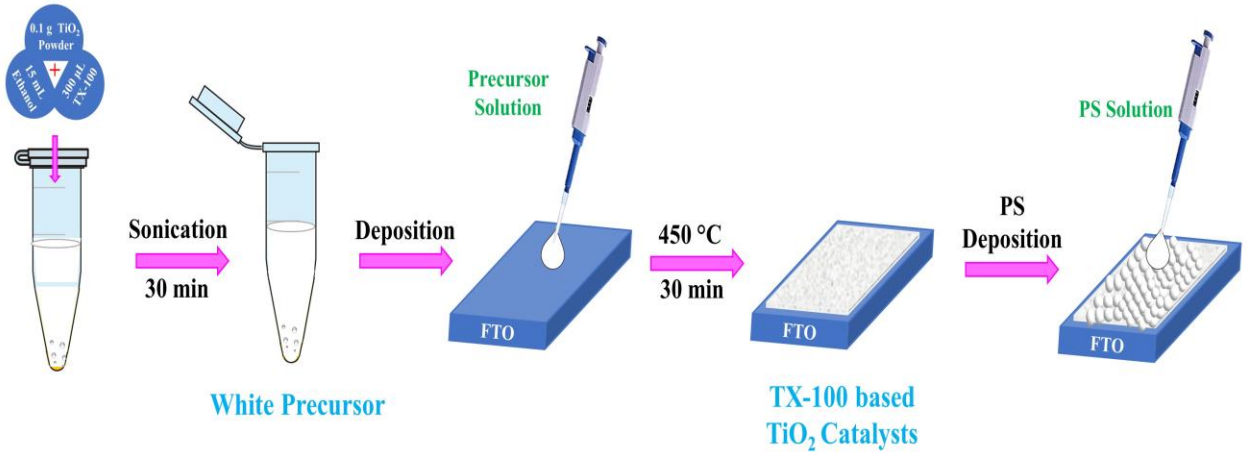

Figure S18. Schematic illustration of photocatalyst fabrication. Related to Figure 4. (At the initial stage, the TiO_2 powder was ground, after getting fine powder ethanol, and Triton X-100 was added to make a precursor solution. This precursor solution was dropped on FTO following the calcination process. A number of the coating can be increased to attain the desired film thickness).

Transparent Methods

Material Growth

Precursor solution of TiO_2 was prepared by grinding the TiO_2 (P25) powder (80 % anatase, and 20 % rutile from Degussa, Germany) in a mortar. The stuck TiO_2 powder inside mortar was removed with a spatula in order to grind aggregates. After getting the fine powder, 1 mL of DI water and 300 μL of Triton X-100 (Sinopharm Chemical Reagent Co., Ltd. China) were added dropwise and ground to make a paste. Triton X-100 was used as a non-ionic surfactant. Furthermore, 15 mL of ethanol (China General Reagent Co., Ltd.) was added dropwise into TiO_2 paste. The obtained precursor solution was sonicated 30 min, stirred for 40 min, and then named as TXT based TiO_2. Ethanol-based TiO_2 (ET) photocatalyst was synthesized by the same method except Triton X-100. Water-based TiO_2 (WT) was prepared by adding only DI water in TiO_2 powder.

Microplastics PS and PE were studied as a model pollutant. They were chosen based on their morphology, environmental abundance, and global production. PS spheres had a smooth surface and a definite size. Different sizes of PS spheres were studied due to their specific size while polyethylene had a rough texture and irregular shaped different sized particles. Microplastics solutions of PS and PE were prepared by the following method. 20 μL of standard concentrated solution of PS spheres (Standard polystyrene microspheres from Huge) were added in 20 mL of DI water and sonicated for 30 min. PE solution was prepared by adding 0.005 g of commercial PE powder (PE-50200 from Shanghai Youngling Electromechanical Technology Co., Ltd. China) in 5 mL of DI water and sonicated for 30 min.

Film Fabrication

The nanoporous WT, ET, and TXT based TiO_2 structures were fabricated on piranha [H_2SO_4: H_2O_2 = 3:1] cleaned FTO glasses (Wuhan Jinge-Solar Energy Technology Co., Ltd. China). The precursor solution of TiO_2 (25 μL) was dropped on conduction side of FTO (covered area 1.25 × 1 cm^2) dried in airflow oven at 70 ℃ and calcined at 450 ℃ for 30 min with a ramping rate of 5 ℃ min^{-1}. The schematic illustration is given in Figure S18.

Characterization

To study the crystal structure of synthesized TXT, ET, and WT based TiO_2 photocatalysts, X-ray diffraction (XRD) analysis was done. XRD spectra were collected by Bruker D8 Advance (XRD) with a Cu Kα radiation value (λ=1.54 Å) ranging from 10° to 70° (2θ) with a scanning speed of 2° min^{-1}. Raman spectrum and imaging were recorded by using the Raman xploRA plus spectrometer (HORIBA), with a green laser (λ = 532 nm) as an excitation source and Raman microscope objective 50x. The morphological characteristics of synthesized catalyst (TXT, ET, WT) and PS spheres were analyzed through field emission scanning electron microscopy (FE-SEM), transmission electron microscope (TEM), and phenom Prox. Each sample was sputtered with gold before SEM analysis. The size of PS spheres was calculated using ImageJ software. To examine the light absorption and optical band gap of fabricated photocatalyst films, the UV–vis absorption spectra were acquired by using a UV–vis diffraction reflection spectroscopy (SHIMADZU UV–2600). Specific surface area and pore-size distribution analysis of prepared TiO_2 films were measured through Brunauer-Emmett-Teller (BET). Amperometric *i-t* curve measurement was performed on an electrochemical station (CHI 660E, Shanghai Chenhua Co., Ltd. China) with a 300 W Xe lamp as a light source (100 mW cm^{-2}). The reactor cell consisted of three electrodes, a working electrode (fabricated film), a counter electrode (Pt wire), and a reference electrode (Ag/AgCl) in 0.1 M solution of Na_2SO_4 electrolyte. The electrochemical impedance spectroscopy (EIS) was also obtained by using the same electrodes and electrolyte solution. The hydrophilicity of films was measured by the contact angle system (POWER EACH, model JC2000DM), and the droplet images were taken through a CCD camera. The chemical state of TiO_2 film was measured via X-ray photoelectron spectroscopy (XPS).

Photodegradation Experiment

For solid-phase degradation, PS spheres solution (20 µL) was dropped on the catalyst films as well as on bare FTO (without catalyst) and dried at room temperature. Two UV lights (each UV light consists of four lamps with 32 W) were used as an artificial light source with a wavelength of 365 nm (3.05 mW cm^{-2}) and 254 nm (4.95 mW cm^{-2}) for the degradation of microplastics. 254 nm

UV light is deeper into the UV spectrum and typically generated about 90 % of the energy as compared to 365 nm. The photodegradation experiment was done in a lamp housing box (35 cm × 25 cm × 15 cm) under the ambient air condition, and the outside temperature was maintained by using a small air fan. The distance between the light source and the samples was 10 cm. All photodegradation experiments were carried out at room temperature without the addition of any oxidant, and each experiment was repeated three times, and average data is presented here.

The liquid phase degradation experiment was carried out by adding 0.05 g of TXT powder in 100 mL of PS solution (100 µL of PS (5 µm size) in 100 mL DI water). The solution was kept for stirring continuously during degradation reaction under 254 nm UV light irradiation, and samples were taken with the time interval.

Detection of Active Species

For the identification of relevant active species formed on the solid (microplastic)-solid (TiO_2) interface under UV light, different scavengers were added, e.g., ethylenediaminetetraacetic acid (EDTA) was used to scavenge the holes (h^+), tert-butyl alcohol (TBA) was used as a hydroxyl radical ($^{\bullet}OH$) scavenger, and the anaerobic experiment was conducted to check the role of oxygen. Briefly, the solutions of 10 mM EDTA and 1000 mM TBA were prepared in 2 mL of PS. 30 µL of PS solution with scavengers (EDTA and TBA) was dropped on TXT film for the detection of active species. Anaerobic hole scavenging experiment was conducted by placing the PS loaded TiO_2 film in an airtight reaction chamber (upper half part made of quartz and button half part made of Teflon, equipped with helical spin structure) under irradiation. Before irradiation, the air was removed from the chamber through the groove, and a vacuum environment was built through injection. The blank test was conducted without a photocatalyst (PS was dropped on cleaned FTO). All films were kept under UV light irradiation for 6 h, and analysis was done through SEM. The photodegradation of PS was observed to check the inhibition effect of these scavengers.

***In-situ* DRIFTS Experiment**

In-situ DRIFTS analysis was done on a Shimadzu FT-IR spectrometer (Tracer-100) armed with

a highly sensitive mercury cadmium telluride detector (MCTD) cooled through liquid nitrogen, and a temperature controller was fixed to the DRIFTS chamber to confirm the constant reaction temperature (Praying Mantis Kit, Harrick). For the *in-situ* DRIFT experiment, TiO_2 nanoparticles were prepared by the following method: TiO_2 precursor solution was dried for 6 h at 120 ℃ and then calcined at 450 ℃ with a ramping rate 5 ℃ min^{-1} for 30 min. The PS/TiO_2 composite was prepared by mixing 20 mL of PS solution (40 µL in 20 mL DI water) in prepared TiO_2 powder and dried at 70 ℃. A small proportion of PS/TiO_2 composite powder was used for DRIFTS experiment. The employed condition was: RH = 85 %, air (100 mL/min), and 365 nm UV light.

Intermediates Detection

The reaction intermediates during the PS degradation were detected by high-pressure photon ionization-time of flight mass spectrometry (HPPI-TOFMS) ion mass analyzer (Wang et al., 2016). The sample was prepared by dropping 40 µL solution of PS on TXT film which was dried at room temperature. For intermediates analysis, the prepared PS loaded TXT film was kept in a reaction chamber (upper half part made up of quartz and button part made up of Teflon, equipped with helical spin structure and the shallow groove) supplied with a continuous airflow under 365 nm UV light for 120 min. Employed relative humidity was 100 % at 25 ℃, and the HPPI-mass spectrum was recorded automatically.

End Product Analysis

Final products of microplastics degradation were analyzed by gas chromatography (SHIMADZU GC-2014). The concentration of end product was expressed in ppm. Sample for GC analysis was prepared by making the composite of 1 g of TiO_2 powder with 700 µL solution of PS and dried at 70 ℃. The obtained powder was put in a designed airtight quartz chamber under 365 nm UV light. Before reaction, the airtight chamber was vacuumed, and pure air was injected in it. Moreover, complete mineralization was examined through thermogravimetric analysis (TGA).

RAMAN Analysis of PE

The degradation of PE was investigated by using Raman xploRA plus spectrometer (HORIBA) following the RAMAN imaging technique, while the RAMAN spectrum was recorded with green laser (λ = 532 nm) as an excitation source. A visual search was done via Raman microscope objective 50x to take the image and spectrum of the selected area of PE with time intervals. Throughout the whole experiment, the same point was selected (all influencing parameters were kept the same) for the analysis of PE degradation

SUPPLEMENTAL REFERENCES

Ariza-Tarazona, M.C., Villarreal-Chiu, J.F., Barbieri, V., Siligardi, C., Cedillo-González, E.I., (2019). New strategy for microplastic degradation: Green photocatalysis using a protein-based porous N-TiO_2 semiconductor. Ceram. Int. 45(7), 9618-9624.

Ariza-Tarazona, M.C., Villarreal-Chiu, J.F., Hernandez-Lopez, J.M., Rivera De la Rosa, J., Barbieri, V., Siligardi, C., Cedillo-Gonzalez, E.I., (2020). Microplastic pollution reduction by a carbon and nitrogen-doped TiO_2: Effect of pH and temperature in the photocatalytic degradation process. J. Hazard. Mater. 395, 122632.

Decker, C., Mayo, F.R., (1973). Aging and degradation of polyolefins. II. γ-initiated oxidations of atactic polypropylene. Polymer Chem. Ed. 11(11), 2847–2877.

Kang, J., Zhou, L., Duan, X., Sun, H., Ao, Z., Wang, S., (2019). Degradation of Cosmetic Microplastics via Functionalized Carbon Nanosprings. Matter 1(3), 745-758.

Karthiga, R., Kavitha, B., Rajarajan, M., Suganthi, A., (2015). Photocatalytic and antimicrobial activity of $NiWO_4$ nanoparticles stabilized by the plant extract. Mater. Sci. Semicond. Process. 40, 123-129.

Satoh, N., Nakashima, T., Kamikura, K., Yamamoto, K., (2008). Quantum size effect in TiO_2 nanoparticles prepared by finely controlled metal assembly on dendrimer templates. Nat. Nanotechnol. 3, 106–111.

Shyichuk, A., White, J.J.J.o.A.P.S., (2000). Analysis of chain‐scission and crosslinking rates in the photo‐oxidation of polystyrene. J. Appl. Polym. Sci. 77(13), 3015-3023.

Tian, L., Chen, Q., Jiang, W., Wang, L., Xie, H., Kalogerakis, N., Ma, Y., Ji, R., (2019). A carbon-14 radiotracer-based study on the phototransformation of polystyrene nanoplastics in water versus in air. Environ. Sci. Nano 6(9), 2907-2917.

Wang, Y., Jiang, J., Hua, L., Hou, K., Xie, Y., Chen, P., Liu, W., Li, Q., Wang, S., Li, H., (2016). High-pressure photon ionization source for TOFMS and its application for online breath analysis. Anal. Chem. 88(18), 9047-9055.